Using 2D Vortex Plasmons/Phonon Polaritons to Control Electronic Selection Rules

by

Francisco Leal Machado

Submitted to the Department of Physics
in partial fulfillment of the requirements for the degree of

Bachelor of Science in Physics

at the

MASSACHUSETTS INSTITUTE OF TECHNOLOGY

June 2016

Signature redacted

Author .....
.....
Department of Physics
May 6, 2016

Signature redacted

Certified by.....
...
Marin Soljačić
Professor of Physics
Thesis Supervisor

Signature redacted

Accepted by .....
Nergis Mavalvala
Senior Thesis Coordinator, Department of Physics

Using 2D Vortex Plasmons/Phonon Polaritons to Control Electronic Selection Rules

by

Francisco Leal Machado

Submitted to the Department of Physics
on May 6, 2016, in partial fulfillment of the
requirements for the degree of
Bachelor of Science in Physics

Abstract

The discovery of orbital angular momentum (OAM) sustaining modes established a new degree of freedom by which to control not only the flow of light but also its interaction with matter. However, OAM sustaining modes have yet to be used to control the quantum dynamics of an electron in an atom or molecule due to the large length scale discrepancy between the wavelength of light and the size of the electron's orbital. In this work, we analyze the interaction between OAM carrying polariton vortex modes (for plasmon and phonon polaritons) and a hydrogen atom, and show that these modes can be used to engineer new selection rules in electronic transitions. Moreover, we show that these selection rules are robust to the displacement of the electronic system away from the vortex center. Perhaps more surprisingly, we find how displacement can be used favourably to tune which absorption process is dominant. Our findings are best suited to vortex modes that can be created in graphene, monolayer conductors, hBN, thin polar dielectrics, and many other polariton-sustaining thin materials. Another platform for observing these effects could be quantum dots interfaced with surface plasmons in conventional metals.

Thesis Supervisor: Marin Soljačić
Title: Professor of Physics

Acknowledgments

First and foremost, I would like to thank my parents and grandparents who supported me from an ocean away, even though they really wanted me to be close to them.

On a similar note, I would like to thank my brother, for always being there, not only as a brother by also a friend, and as (grand)son and a half for my (grand)parents when I was away.

Remaining in the same geographical location, I would like to thank my friends back home, for their support, for their enthusiasm, and for always welcoming me with open arms, despite me being on a different continent 50 weeks a year.

To the many professors, too many to enumerate, that showed me that science is not only fun but what I want to think about for the rest of my time in this planet, I thank you.

Yet, I would like to address a few people specifically, in chronological order, Prof. Rui Travasso, Prof. Mark Vogelsberger, Prof. Pablo Jarillo-Herrero, Dr. Homer Reid and Prof. Marin Soljačić for welcoming me into the world of their research. Diving into the deep end of research has been an amazing experience not only to learn valuable skills and amazing physics, but also to explore different branches of this vast subject and help me understand what I want to study in the future. I would also like to thank, in no particular order, Dr. Paul Torey, Yafang Yang, Dr. Efren Navarro-Moratalla, Dr. Joel Wang, Valla Fatemi, Melis Tekant, Daniel Rodan, Dr. Landry Bretheau and Dr. Yaqing Bie for the guidance and help making my experience in research even more insightful and fun.

This work was only possible with the help and the guidance of Dr. Ido Kaminer, for whom I am very thankful for the time, energy and knowledge he shared with me for these past two semesters. Although an undergraduate, Nicholas Rivera's knowledge and enthusiasm were an tremendous help and source of inspiration, and for that I thank him too. I would also like to thank Hengyun (Harry) Zhou, Sruthi Narayanan and Elise Newman for proofreading and helping me improve this thesis.

What made my experience at MIT so much more than academics were the people

I met along the way. I would like to thank the friends that I made in this amazing place, who pushed me both academically and personally to become a better version of myself. May our paths continue intertwined for the rest of our lives.

On to the Physics now!

Contents

List of Figures

Chapter 1

Introduction

1.1 Overview and Motivation

Electronic transitions in atomic systems have played a major role in Physics providing a powerful tool for understanding many fundamental questions, including sparking the ideas that led to Quantum Mechanism. As a result, understanding and controlling electronic transitions is an important problem not only in probing the foundations of quantum mechanics, but also as a means to uncover new physical phenomena. In the quest for new and controllable light matter interactions, the discovery of orbital angular momentum of light (OAM) has made a new degree of freedom available with which to engineer electronic transitions. However the mismatch between the length scales of electronic systems and the wavelength of light has prevented such transitions to be experimentally meaningful. In a different area of Physics, surface polariton (SP(h)P) modes, electromagnetic modes of radiation highly confined to the surface of a material, have been extensively studied due to their variety of applications like light based devices, radiation sources, novel energy transfer mechanisms at the nanoscale and protein sensing.

In this work we combine the concepts of OAM and SP(h)P modes and add controllable high Δm transitions to the list of possible application of SP(h)Ps by presenting a new formalism for light-matter interaction with highly confined OAM carrying SP(h)P vortex modes. We show that these modes enable new selection rules for

electronic transitions based on the conservation of angular momentum and explain how they enable a new degree of control over atomic selection rules. We also present the robustness of this scheme by studying the effect of off-axis displacements of the atom relative to the center of a polaritonic vortex, and study how the dominance of different absorption processes depends on the radial displacement of the atom. We find that the increase of confinement is associated with a decrease of the length scale of the system, resulting in a trade-off between greater electronic absorption rates and a more robust experimental setup. This is of particular interest in 2D conductors like graphene where the confinement factor of these polaritonic excitations can be externally tuned [6, 15].

1.2 Thesis Structure

This thesis is composed of 5 chapters. In chapter 2 we present an overview of the main background concepts of orbital angular momentum (OAM), surface polarition modes (SP(h)P) and atomic transitions required for the remainder of this work. Chapter 3 describes OAM carrying SP(h)P vortex modes and analyzes transition rates between different electronic states due to the absorption of a single vortex mode when the atom is at the center of the vortex mode. In this configuration we show the existence of a selection rule based on the conservation of angular momentum. This work is generalized in Chapter 4 where the atom is displaced from the center of the vortex. In this more general configuration, we show that the atom centered selection rule no longer applies, but that the angular momentum conserving transition is robust for small displacements of the atom. We also describe how the displacement of the atom from the center of the vortex mode enables new absorption processes to become dominant in a predictive way. In this chapter we also study the impact of the confinement of our surface polariton mode on the properties of the system and show the existence of a balance between an increase in the absorption rate and a decrease in the length scale of the experiental system. Chapter 5 summarizes the work presented and suggests future directions and applications.

Chapter 2

Background Overview

In this chapter we introduce the main background concepts from which the work presented in this thesis was built upon. The concept of orbital angular momentum is introduced and is related to the possibility of new, yet unobserved electronic transitions in electronic systems. Surface polariton modes are then discussed with emphasis on their properties, conditions for existence and electromagnetic field profile. Finally, a brief introduction to Fermi's Golden Rule and the dipole approximation is made to provide context for the calculations made later in this thesis.

2.1 Orbital Angular Momentum

The concept of orbital angular momentum (OAM) of light was first introduced by Allen *et al.* [1] in 1992. By studying Laguerre-Gaussian modes of light, with an azimuthal dependence of $e^{il\phi}$, the authors showed that the ratio of the flux of angular momentum and the power of the mode were consistent with angular momentum of $\hbar l$ being carried by each photon. The first experimental verification of light carrying OAM was performed by He *et al.* [19] in 1995, however the experiment did not demonstrate OAM was carried at the single photon level. More recent work in quantum optics demonstrated that OAM is indeed carried by a single photon and is not an ensemble effect of many photons [29], establishing a new degree of freedom with which to control the flow of light and its interaction with matter at the single particle

level.

The generality and power of OAM as a platform for novel light-matter interaction can be understood by the numerous applications that have been developed in recent years, which include angular velocity measurement [27], higher bandwidth communication using novel OAM multiplexing techniques [51, 48], new quantum information systems [33], quantum memories [35] and quantum sources of entanglement [29] with applications to quantum cryptography implementations [32]. The same concept of granting OAM by shaping the phase profile of light has been extended to the Schrödinger wave function for electrons with applications in beam physics [3, 46, 47, 25].

Spectroscopy is an area where the application of OAM can open new possibilities, but which has yet to be explored. The existence of extra angular momentum, beyond a photon's intrinsic spin of $\hbar$, has the potential of enabling new and controllable electronic transitions in atom-like systems including atoms, molecules and artificial atoms like quantum dots. However, the new transitions are not expected to be experimentally meaningful since "even when compared with a tightly focused beam, the effective cross section of the atom is extremely small; so the helical phase front is locally indistinguishable from an inclined plane wave" [52]. In other words, the length scale mismatch between the radiation and the electronic system prevents the electron to couple to multipole moments of radiation beyond dipole, restricting the possible set of transitions it can undergo. In the dipole approximation, ubiquitous in light-matter interaction literature, the only allowed transitions require a change in quantum numbers of $\Delta l = \pm 1$ and $\Delta m = 0, \pm 1$ (a more detailed discussion can be found in Appendix B). In order to use OAM to explore new electronic transitions it becomes critical to match the photonic and electronic length scales. Surface polaritons bridge that length scale gap.

2.2 Surface Polaritons Modes

Surface polariton (SP(h)P) modes, highly confined modes of light at the interface between two materials, have excited the scientific community as they enable novel phenomena to occur and be explored. These confined modes of light arise from the oscillations of electrons (plasmons) or lattice vibrations (phonons) at the surface of the material, forming a single excitation called surface plasmon polaritons (SPPs) and surface phonon polaritons (SPhPs) respectively. Although SPP and SPhP modes arise from very different physical mechanisms, both can be understood through the linear response functions of the material, the electric permittivity ϵ and the magnetic permeability μ, resulting in the same description of their electromagnetic field profiles. As a result, the two phenomena can be unified within the umbrella of surface polaritons.

In this chapter we introduce the SPP and SPhP modes, and discuss their properties as an introduction to the rest of the work developed.

2.2.1 Surface Plasmon Polaritons

First introduced in 1952 by Pines and Bohm [38], a plasmon is an oscillatory excitation of the electron density in a material, which arises from the Coulomb interaction between the electrons in the material. The motion of the electrons generates an oscillating electromagnetic field and the two components (electromagnetic field and electron oscillation) composes the plasmon, or plasmon polariton.

Although the initial study considered excitations in the bulk of a material, previous studies by Zenneck [53] and Sommerfield [43] had looked into the oscillation of electrons at the interface of a material. Nevertheless, Ritchie [39] in 1957 was the first to consider surface electron oscillations as a type of plasmon mode and coin the term of "surface plasmons", also known as surface plasmon polaritons (SPPs).

In the years between Ritchie's paper and today, much work has been devoted to SPP modes due to the profile of their electromagnetic field, in particular its accessibility and confinement. Unlike bulk plasmons, the electromagnetic fields are confined

near the surface of the material, extending evanescently out of the material, which enables outside radiation to excite the mode. This confinement occurs not only in the out-of-plane direction but also the in-plane direction, where the field's wavelength is much smaller than equally energetic free space radiation, enabling phenomena to occur at lengths smaller than the diffraction limit (more details in Section 2.2.3).

These two properties of SPP, accessibility and confinement, enable a whole new set of applications which include, but are not limited to, more efficient energy transfer mechanisms [42, 21], plasmon based protein sensors [41], radiation sources [26, 24, 50, 2] and light-based computational devices [37].

2.2.2 Surface Phonon Polaritons

The phonon corresponds to a vibration of a crystal's lattice, responsible for many processes of energy dissipation within the crystal. It was first proposed as a quantized excitation by Einstein in 1906 [14] when he applied the concepts recently proposed by Max Planck to vibrations in solids in order to explain their heat capacity at low temperatures. Studied extensively in the previous century, recent interest has arisen in surface phonons polaritons (SP(h)Ps) because, similarly to SPPs, an evanescent electromagnetic mode is present, enabling interesting applications like enhanced energy transfer at the nanoscale distance [20, 42].

However, since they correspond to very different physical mechanisms within a solid, SPhP and SPP yield different dispersion relations and operate at very different frequencies, infrared and visible/ultraviolet respectively. Moreover SPhP usually have lower losses, opening the possibility of longer propagation lengths, of interest in telecommunication and nanophotonic applications [4].

2.2.3 Surface Polaritons at a Single Interface

Being interested in the electromagnetic profile of these modes, in this section we describe SP(h)P modes at the interface of two materials, as pictured in Fig.(2-1). In particular we study the transverse magnetic (TM) modes, where the magnetic field

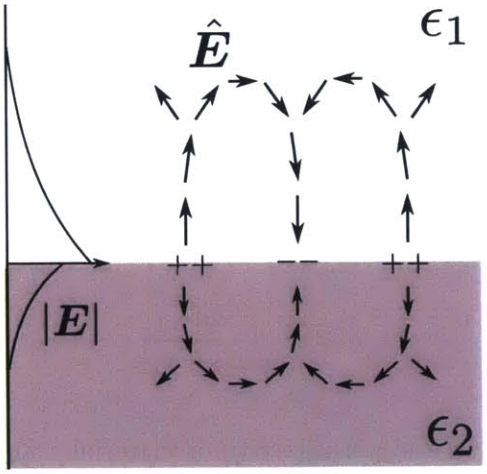

Figure 2-1: **SP(h)P mode at the interface of two materials with dielectric permittivities of ϵ_1 and ϵ_2.** The oscillation of electron density/lattice at the interface leads to the generation of a electromagnetic excitation that propagates along with the electron oscillation. The arrows correspond to the mode profile, while on the left, the exponential decay associated with the evanescent nature of the field is pictured.

is parallel to the surface, as they are the only ones supported in parabolic materials, although transverse electric (TE) modes have been predicted for graphene [31]. Despite the wavelength of SP(h)P modes being much smaller than free space radiation of the same energy, it is still much larger than the unit cell of typical solids. As a result, the response of the material is well characterized by the macroscopic response functions of the material ϵ and μ and the atomistic details can be ignored. However, in real materials the difference between magnetic permeabilities is very small, so, for the remainder of this work, we take all magnetic permeabilities to equal the vacuum's permeability μ_0. Another assumption used throughout this work is that we are working in the lossless limit, meaning that the imaginary part of ϵ is zero. Details of the derivations in this section can be found in Appendix A.

Considering the single interface geometry between two materials, as depicted in Fig.(2-1), the vector potential of planar SP(h)P is given in the electrostatic limit, by [22]:

$$\boldsymbol{A} = \frac{A_0}{\sqrt{2}} \left(\hat{q} + i\hat{z}\right) e^{-qz} e^{i(\boldsymbol{q}\cdot\boldsymbol{\rho} - \omega t)} \tag{2.1}$$

where A_0 is the overall magnitude of the field, $\boldsymbol{q}$ is the in-plane momentum of the mode, $\hat{z}$ is the out-of-plane direction, $\boldsymbol{\rho}$ is the in-plane position, ω is the frequency of the mode, and hats correspond to unit vectors.

The dispersion relation, which relates $\boldsymbol{q}$ and ω, is given by the dielectric function of the materials at the interface as [22]:

$$q \approx \frac{\omega}{c}\sqrt{\frac{\epsilon_{r1}\epsilon_{r2}}{\epsilon_{r1}+\epsilon_{r2}}} \tag{2.2}$$

where ϵ_{ri} is the relative electric permittivity of material i and c is the speed of light in vacuum.

One of the requirements for the existence of SP(h)P plane modes (as mentioned in Appendix A) is that ϵ_1 and ϵ_2 must have opposite signs, which can be obtained if one of the materials is a metal and the other a dielectric. Moreover, since we are interested in propagating modes, with q real, we also require $\epsilon_{r1} + \epsilon_{r2} < 0$. Since ϵ_{r1} and ϵ_{r2} have opposite signs the denominator of Eq.(2.2) may be much smaller than the numerator leading to an in-plane momentum q much larger than the free space momentum of light ω/c.

2.2.4 Surface Polaritons in Thin Film Materials

We now consider a slab of a metallic material surrounded by a dielectric above and below (which may be different), as pictured in Fig.(2-2). For a large slab thickness we expect both interfaces to support SP(h)P modes. As we decrease the thickness of the material, these two modes will begin to hybridize. Surprisingly, in the limit as the thickness goes to 0, only the TM mode is allowed [22], whose profile can be computed with an ansatz similar as in the single interface case (more details in Appendix A).

Although the field profile of the mode in the dielectric matches the result we obtained in the single interface case, the SP(h)P dispersion relation now depends on the conductivity of the metal film as well as the dielectric constants of the surrounding

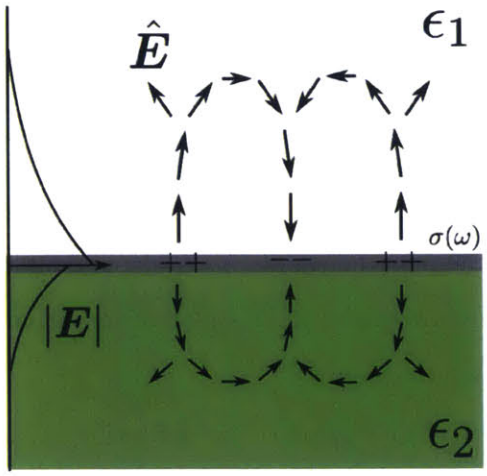

Figure 2-2: **SP(h)P mode at a thin metallic film surrounded on top(bottom) by a dielectric with electric permittivity $\epsilon_1(\epsilon_2)$.**The electric field parallel to the thin field generates a surface current in the film, as a result ϵ_1 and ϵ_2 need not have have opposite signs. The arrows represent the field's direction while on the left its magnitude is pictured.

dielectrics in the following form (in the electrostatic limit):

$$q \approx \frac{\epsilon_{r1} + \epsilon_{r2}}{2} \frac{2i\omega}{\sigma(\omega, q)} \tag{2.3}$$

where $\sigma(\omega, q)$ is the frequency and momentum dependent conductivity of the metal.

Although the formalism and approach presented in this work is general, of particular experimental interest are monolayers of metals or 2D materials, like graphene, as they can be placed on top of a SiO_2 substrate. This 2D geometry enables the development of integrated on-chip solutions with potential applications in novel computational frameworks beyond electronics. The conductivity in this class of materials in the SPP mode regime can be obtained through the Drude formulation which yields [23]:

$$\sigma_{metal} = \frac{n_V e^2}{m^*} \frac{i}{\omega + i\tau^{-1}} \quad \text{and} \quad \sigma_{graphene} = \frac{e^2 v_F \sqrt{n_s}}{\sqrt{\pi}\hbar} \frac{i}{\omega + i\tau^{-1}} \quad \Rightarrow \quad \sigma \propto \frac{1}{\omega} \tag{2.4}$$

where n_V (n_s) is the volume (surface) number density of electrons, m^* is the effective mass of the electron, v_F the Fermi velocity in graphene, e the charge of the electron

and $2\pi\hbar$ is Planck's constant.

More generally, the dispersion relationship for an isotropic material can be written as:

$$q = \eta(\omega)\frac{\omega}{c} \tag{2.5}$$

where η, called the confinement factor, is an ω dependent dimensionless parameter which corresponds to the ratio of the wavelength of radiation in free space and of the SP(h)P mode, for the same frequency.

The value of η provides a figure of merit for analyzing the length scale change when free radiation is coupled in SP(h)P modes, as well as, for comparing different SP(h)P supporting materials. The range of relevant materials and associated confinement factors is vast and includes SPhP modes in SiC, where η can experimentally reach values of 200 [4]; SPhP modes in hBN, where η has been experimentally observed to be near 100 [5] and where theoretical upper bounds are greater than 1000 [45]; SPP modes in monolayer films of metals like silver and berylium, where η can reach values around 300 [34] and 350 [12], respectively; and SPP modes in graphene, where measurements of η fall in the range of 150-240 [22, 28, 49, 16] for different regimes and where theoretical upper bounds are around 300 [22].

The large confinement of the electromagnetic field bridges the length scales between the photonic modes and the size of electronic systems, providing the framework for electronic transitions beyond the dipole approximation [40].

2.3 Electronic Transitions in Atoms

Having described the background of SP(h)P modes, we address the formalism behind the computation of transition rates between electronic states of the atom. In this section the Hamiltonian of the system composed of the electron and the electromagnetic field is presented, Fermi's Golden Rule is discussed as a perturbative method for computing the transition rates, and the selection rules arising from the interaction of an atomic system with free space radiation are discussed.

2.3.1 Hamiltonian of the System

The last piece of theoretical machinery necessary to understand the electronic transitions due to SP(h)P mode absorption is the description of the quantum dynamics of the system, expressed by its Hamiltonian. There are three components of the Hamiltonian that need to be included, that of the electronic system, the electromagnetic field, whose information is encoded in the vector potential, and the interaction between the two. In this work we consider the non-relativistic Hamiltonian for a charged particle interacting with a electromagnetic field, given by [8]:

$$H = H_{atom} + H_{field} + H_{int} \quad \text{where} \tag{2.6}$$

$$H_{atom} = \frac{\mathrm{p}^2}{2m} + V(\boldsymbol{r}) \quad , \quad H_{field} = \sum_i \hbar\omega_i \left(a_i^\dagger a_i + \frac{1}{2}\right) \tag{2.7}$$

$$H_{int} = \frac{e}{2m}\left(\boldsymbol{A}\cdot\boldsymbol{p} + \boldsymbol{p}\cdot\boldsymbol{A}\right) + \frac{e^2}{2m}|\boldsymbol{A}|^2 \tag{2.8}$$

where H_{atom} is the Hamiltonian of the electronic system, in this work assumed to be the hydrogen atom, with $V(\boldsymbol{r})$ corresponding to the Coulomb interaction between the proton and the electron. $\boldsymbol{A}$ is the field operator, $\boldsymbol{p}$ is the momentum operator, $a_i^\dagger$ is the creation operator of a SP(h)P with frequency ω_i and m is the mass of the electron. For the remainder of this work we will be working in a gauge where the potential of the external radiation is zero, $\phi(\boldsymbol{r}) = 0$. H_{field} corresponds to the Hamiltonian of the electromagnetic field. In this quantum field approach, $\boldsymbol{A}$ is promoted to an operator as:

$$\boldsymbol{A} = \sum_i \alpha_i \left(\boldsymbol{e_i} a_i + \boldsymbol{e_i^*} a_i^\dagger\right) \tag{2.9}$$

where α_i is a normalization constant (discussed in more depth in Appendix C.2), dependent on the field profile of the mode $\boldsymbol{e_i}$. α_i has units of vector potential, while $\boldsymbol{e_i}$ is dimensionless.

2.3.2 Fermi's Golden Rule and Transition Rates

We want to study the quantum dynamics of the electron in this system, so we take the unperturbed Hamiltonian $H_{atom} + H_{field}$ and consider H_{int} a perturbation on the system, assuming the field strength to be small. In this regime we can neglect the contributions from the $|\boldsymbol{A}|^2$ term. Another, more field theoretical explanation, is to say we are only considering 1 SP(h)P processes, while $|\boldsymbol{A}|^2$ corresponds to a 2 SP(h)P mechanism.

The calculation of the transition rates between the different electronic states through the absorption of a SP(h)P mode is obtained through Fermi's Golden Rule, which is given by:

$$\Gamma = \frac{2\pi}{\hbar}|\langle t_f|H_{int}|t_i\rangle|^2\rho(\hbar\omega) \tag{2.10}$$

where $|t_i\rangle$ is the entire quantum state of the system, given by $|s_i\rangle \otimes |n_\omega\rangle$, where $|s_i\rangle$ is the electronic state of the electron, while $|n_\omega\rangle$ is the state of the field, given by n SP(h)P excitations with frequency ω; and $\rho(\hbar\omega)$ is the the density of states of the SP(h)P modes with energy $\hbar\omega$.

In order to compute the interaction between the atomic and photonic systems knowledge of the solutions to the unperturbed systems is required. The solution to the photonic OAM carrying vortex modes is addressed in Chap.(3), while the solution to the atomic part of the problem can be found in any introductory Quantum Mechanics textbook like [17, 7], and are simply quoted here:

$$\begin{aligned}\langle \boldsymbol{r}|n,l,m\rangle &= \psi_{nlm}(\boldsymbol{r}) = \\ &= e^{-r/na_0}\left(\frac{2r}{na_0}\right)^l\sqrt{\left(\frac{2}{na_0}\right)^3\frac{(n-l-1)!}{2n(n+l)!}}L^{2l+1}_{n-l-1}(2r/na_0)Y^m_l(\theta,\phi)\end{aligned} \tag{2.11}$$

$$\langle n,l,m|\hat{H}|n,l,m\rangle = -\frac{13.6\,\mathrm{eV}}{n^2} \tag{2.12}$$

where n, l, m are the quantum numbers used to label the bound states. l and m are related to the total angular momentum and the projection of the angular momentum

onto one direction, chosen to be $\hat{z}$, by:

$$\langle n,l,m|\hat{L}^2|n,l,m\rangle = \hbar^2 l(l+1) \quad \text{and} \quad \langle n,l,m|\hat{L}_z|n,l,m\rangle = \hbar m \tag{2.13}$$

The simplification of Eq.(2.10) for our particular application is done in Appendix D.

2.3.3 Dipole Approximation and Selection Rules

Although Eq.(2.8) is the precise interaction Hamiltonian, in most cases it can be simplified. This simplification arises whenever there is a great length scale mismatch between the light wavelength and the size of the atomic system. As a result, the electron only "sees" a constant electromagnetic field in the volume of its orbital so the interaction Hamiltonian can be simplified.

In the case of the hydrogen atom, the size of the orbital is of order of the Bohr radius $a_0 \approx 5.29 \times 10^{-11}\,\mathrm{m}$, while the difference between energy levels is at most $13.6\,\mathrm{eV}$, which corresponds to a wavelength of $\lambda = 9.116 \times 10^{-8}\,\mathrm{m}$, which is 500 times larger than a_0.

This approximation is known as the dipole approximation, because the interaction between the field and the electronic system is simplified to the electric dipole matrix element dotted with the, approximately constant, electric field at the location of the atom (more details in Appendix B):

$$H_{int} = -\boldsymbol{E}_0 \cdot (e\boldsymbol{r}) \tag{2.14}$$

This simple interaction constrains the possible electronic transitions, such that the the change of quantum numbers in the transitions is given by:

$$\Delta l = \pm 1 \quad , \quad \Delta m = \pm 1, 0 \tag{2.15}$$

Chapter 3

Electronic Transitions in a Vortex Centered Atom

In this chapter we describe OAM carrying vortex modes and study the transitions rates of an electron associated absorption of one of these SP(h)P modes, pictured in Fig.(3-1). In this chapter we consider atoms which are located exactly at the center of the vortex mode and analyze how electronic transitions can be engineered by designing the correct vortex mode supporting substrate. We focus our attention to the family of transitions between initial principal quantum number 5 and final quantum number 6 as there are many dipole allowed and forbidden transitions, providing plenty of examples of the phenomena we are describing. Nevertheless, the phenomena described here are completely general to other transitions in the hydrogen atom and should translate to more complex atomic systems. More details on the calculation or numerical code used can be found in Appendix D.

3.1 Description of Vortex Mode

A OAM carrying vortex mode can be obtained as the superposition of planar modes coming from different angles with a phase shift linearly dependent on the incoming angle θ. Experimentally this can be done by having the optical path increase with incoming angle, as described in experiments [44, 10, 11]. Since the phase shift must

match at each point modulus 2π, the vortex mode can be labeled by the winding number m of its phase shift around a circle. The resulting radiation profile can be written analytically as:

$$\begin{aligned}\boldsymbol{A}_m = \frac{1}{2\pi}\int d\theta\, A_{\boldsymbol{q}} e^{im\theta} = \frac{A_0}{2\sqrt{2}} e^{-i\omega t} i^{m-1} e^{im\phi} e^{-qr\cos(\theta)} \times \\ \times \Big\{ 2J_{-m}(q\rho)[\hat{r}\cos(\theta) + \hat{\theta}\sin(\theta)] + im\sqrt{2}\frac{J_{-m}(q\rho))}{q\rho}\hat{\phi} \\ +(J_{-1-m}(q\rho) - J_{1-m}(q\rho))[\hat{\theta}\cos(\theta) - \hat{r}\sin(\theta)]\Big\}\end{aligned} \tag{3.1}$$

where $\boldsymbol{A_q}$ is the plane SP(h)P mode described in Eq.(A.8) with linear momentum $\boldsymbol{q}$, θ corresponds to the angle between $\boldsymbol{q}$ and some reference direction $\hat{t}$, set, without loss of generality, to be $\hat{x}$, and $J_\nu(x)$ is the ν-th degree Bessel function of the first kind. The full derivation is contained in Appendix C, in agreement with the prediction in [13] for graphene plasmons.

For the case of silver and gold plasmonic structures, these modes have been observed via SPPs using slit based coupling [11, 10]. The same procedure should be applicable to other classes of plasmonic materials, where the confinement factors are larger. It should also be applicable to materials sustaining SPhP, even though such vortex modes have yet to be observed.

In order for our fully quantum formalism to be valid we need to properly normalize the vortex modes. This normalization, derived in Appendix C.2 enables us to write the field operator for SPP vortex modes as:

$$\boldsymbol{A} = \sum_{q,m} \sqrt{\frac{\hbar q^2}{4\epsilon_0 \bar{\epsilon}_r L\omega}} \left(\boldsymbol{e}_{q,m} a_{q,m} + \boldsymbol{e}^*_{q,m} a^\dagger_{q,m}\right) \tag{3.2}$$

where $\boldsymbol{e}_{q,l}$ are the dimensionless field profiles defined in Eq.(C.9), $\bar{\epsilon}_r$ is the average of the dielectric constant of the materials above and below, ϵ_0 is the electric permittivity of vacuum and L is the radius of the mode.

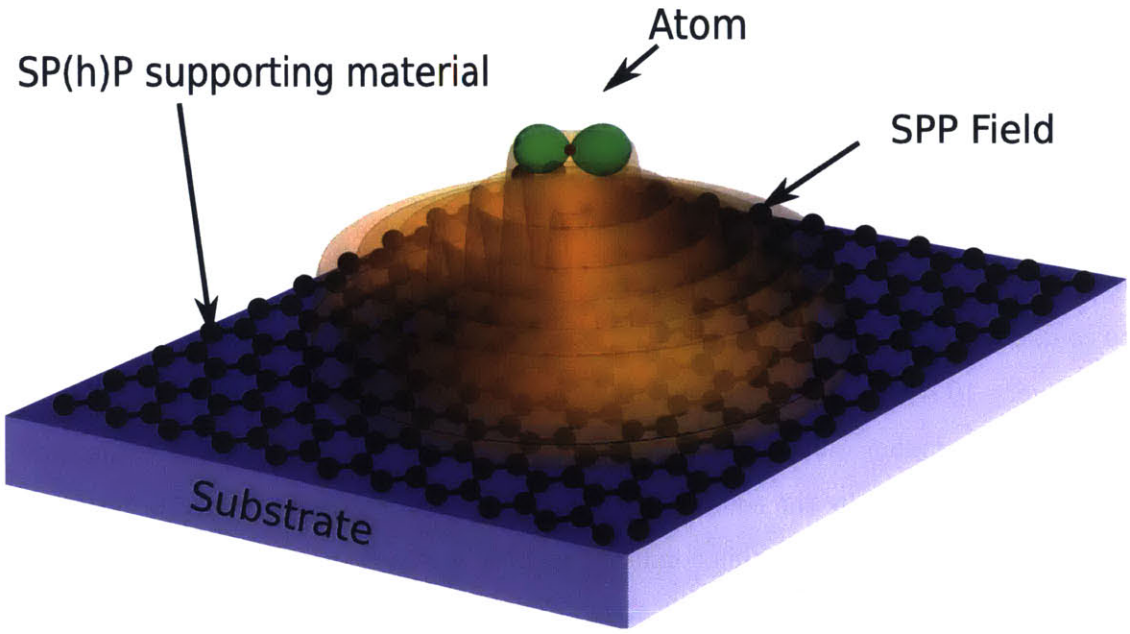

Figure 3-1: **Schematic of the system composed of an electronic system and OAM carrying vortex mode.** An atom is placed a height z_0 above a surface which supports OAM carrying SP(h)P vortex modes. Due to the evanescent nature of the polaritonic mode the atom must be within 10's of nm from the surface of the material.

3.2 Absorption Rates of OAM SP(h)P vortex modes

Computing the absorption rate for the atom centered with the vortex mode center, we obtain the results shown in Fig.(3-2). These results make evident the selection rules associated with the conservation of angular momentum:

$$\Delta m = m_{vortex} \tag{3.3}$$

where $\hbar\Delta m$ is the change in z-projected angular momentum of the electron and $\hbar m_{vortex}$ is the angular momentum of the vortex mode. By generating a single SP(h)P vortex mode, we are able to control the electronic transitions of the atom, for arbitrarily large values of m_{vortex}. This selection rule is exact and arises from the requirement that the azimuthal phase term of the mode ($e^{im_{vortex}\phi}$) and the orbital wavefunction product ($e^{-i\Delta m\phi}$) must cancel. This (mis)match of phase between the vortex mode and atomic degrees of freedom is schematically illustrated in the phase plots **c)** and

b), respectively, on the right side of Fig.(3-2), each corresponding to different highlighted transitions on the left plot.

The impact of the confinement factor η on the transitions rates is also of importance as it guides the choice of material for possible future experiments. Its increase leads to an increase in the absorption rate by many orders of magnitude, as the system moves further away from the dipole approximation and the electron orbital is allowed to couple to higher multipole modes of radiation, enabling processes that would occur once every 10's of millions of years, to occur once every 10's of μs. The access of the system to higher multipole modes of radiation means that the allowed transitions are only constrained by the conservation of angular momentum described in Eq.(3.3). All the transitions fulfilling this condition yield non-zero transition rates, albeit with different magnitudes.

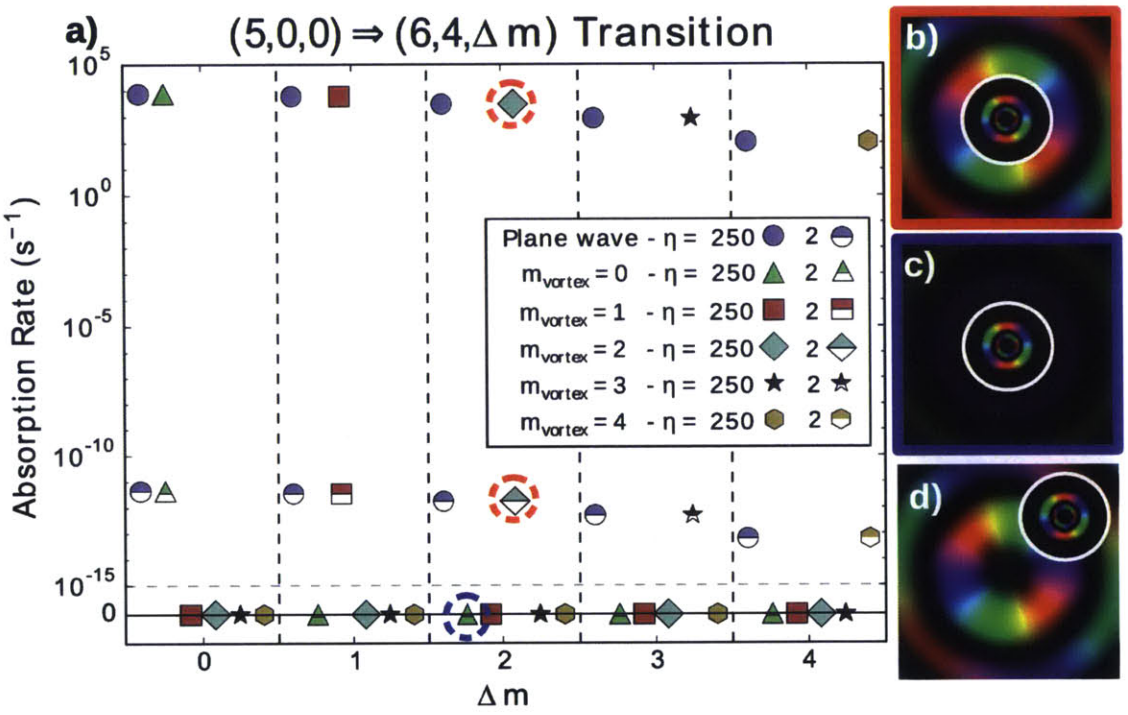

Figure 3-2: **Single photon absorption rates due to absorption of a plane SP(h)P and OAM carrying vortex SP(h)P for different transitions in the family $(5,0,0) \rightarrow (6,4,\Delta m)$ for two different values of confinement, 2 and 250, with $z_0 = 10\,\text{nm}$. a)** The vortex modes impose selection rules on the electronic transitions, while the increase in confinement factor leads to an improvement of the absorption rate by a factor of $\sim 10^{15}$, increasing the rate of occurrences from once every 10's of millions of years to once every 10's of μm. **b)** and **c)** correspond to the phase plots of the highlighted transitions of equal color, where the inside (outside) of the circle corresponds to the electron orbital components (vortex mode). The size of the atom was artificially increased tenfold for illustration purposes. **d)** corresponds to the phase portrait of an atom displaced from the center of the vortex mode where rotational symmetry has been broken, discussed in detail in Chap.(4). Although free space OAM carrying radiation impose the same selection rules, the difference in length scales between radiation and the atom size results in absorption rates too small for experimental observation when the confinement factor η is of order unity. On the other hand with SP(h)P modes the rates for these processes become experimentally meaningful.

Chapter 4

Electronic Transitions in a Displaced Atom

The results presented in Chap.(3) depend on the rotational symmetry of the system around the vortex mode center. In this chapter we consider the case when the atom is no longer aligned with the vortex center, first describing a displaced vortex mode in a convenient way and computing the associated absorption rates. We show that, although the selection rule obtained in Chap.(3) are no longer exact, the transition with $\Delta m = m_{vortex}$ is dominant over a displacement of the length scale of the vortex mode, instead of the length scale of the electronic system, as one would intuitively consider. We also show that as we increase the displacement of the atom, the dominant transition changes in a simple and predictable way. As a result, a single vortex mode can be used to investigate many different new absorption transitions. In this chapter we also discuss the effect of the confinement factor on the transition rates as a function of the distance, showing that there is a trade-off between a greater absorption rate and a more robust experimental setup.

4.1 Displaced Vortex SP(h)P Modes

In order to study transitions rates for an atom displaced from the vortex center, it is more convenient to consider the vortex mode to be displaced from the atom, as

a vortex mode displaced by $-\boldsymbol{D}$ can be written as a superposition of vortex modes centered around the atom, as described in Eq.(C.18):

$$\boldsymbol{A}_m^{-\boldsymbol{D}} = \sum_{n=-\infty}^{\infty} i^{n-m} e^{-i(n-m)\phi_0} J_{n-m}(qD) \boldsymbol{A}_n \tag{4.1}$$

where ϕ_0 is the angle $\boldsymbol{D}$ makes with $\hat{t}$. This amazing property means that the transition rate of the atom by virtue of the displaced vortex can be understood through the transition rates for the atom centered vortices.

4.2 Absorption Rates in a Displaced Atom

Intuitively, we expect the angular momentum selection rule in Eq.(3.3) to not apply when the atom is displaced because angular momentum conservation is related to rotational invariance, which the displacement of the atom breaks. Mathematically, this intuition manifests itself in the fact that a displaced vortex is a superposition of vortices with all possible angular momenta, as described in Eq.(4.1). The impact of the atom's displacement from the vortex center is presented in Fig.(4-1) and Fig.(4-2) for transitions in the family $(5,0,0) \rightarrow (6,l,m)$.

Consider a vortex mode with OAM $\hbar m_{vortex}$ displaced by $\boldsymbol{D}$ from our atomic system. From Eq.(4.1), the magnitude of the overlap integral between the displaced mode and a vortex mode with OAM $\hbar n$ centered with the atom is given by $|J_{n-m_{vortex}}(qD)|$, where q is the mode's momentum. As a result, the transition rates of the displaced atom can be understood based on the transition rates of the axially symmetric case. For special values of D where $J_{n-m_{vortex}}(qD) = 0$, a transition of $\Delta m = n$ is truly forbidden, meaning that there are concentric rings surrounding the vortex for which certain transitions are exactly forbidden.

The transitions rates from a system initially in the state (5,0,0) as a function of the distance D from the vortex center are studied in the left column of Fig.(4-1), each row corresponding to a different value of OAM $\hbar m_{vortex}$ carried by the vortex mode. As expected, for $D = 0$ the selection rule Eq.(3.3) is always satisfied, however

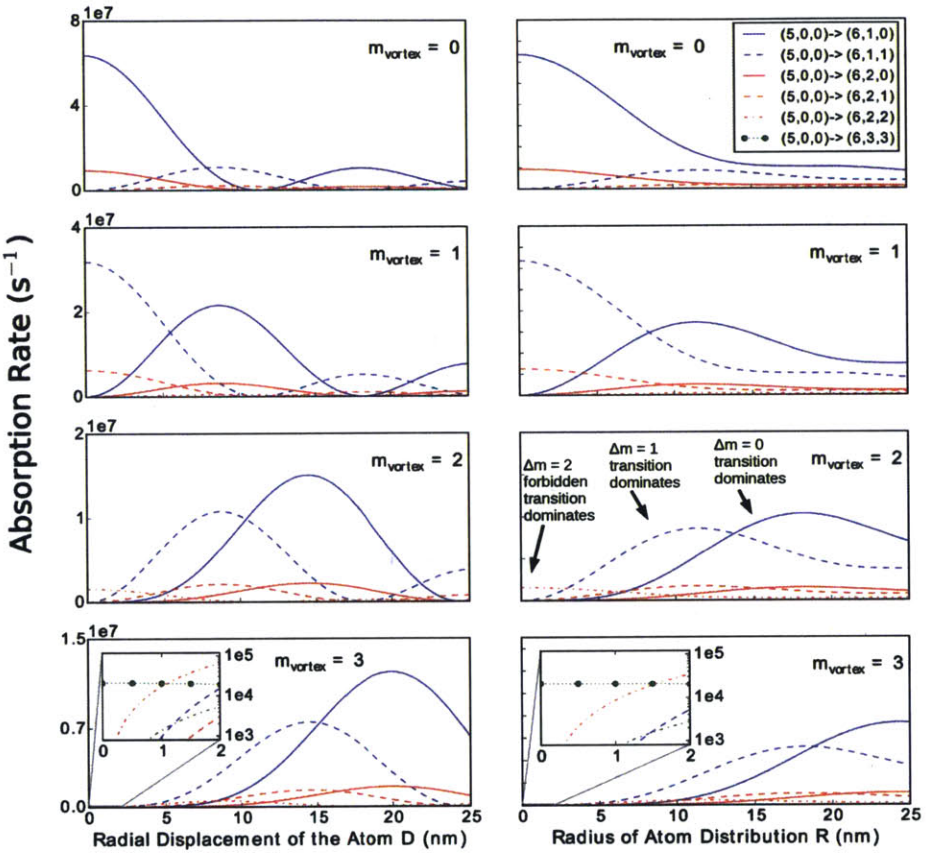

Figure 4-1: **Dependence of the single photon absorption rates of a displaced individual atom (left column) and normalized uniformed atomic distribution (right column) for transitions with initial state $(5,0,0)$ and final principal quantum number 6 at a confinement factor of $\eta = 250$ with z_0 nm.** As the rotational symmetry is broken, the selection rules discussed in Fig.(3-2) are no longer valid and all Δm transitions become allowed. As a result, the geometry of the experiment, including the position of the atom, is of great importance to accurately predict the observed transition. On the left column, the absorption rate of a single atom is plotted for different vortex OAM ($\hbar m_{vortex}$) as a function of the displacement D of the atom. The results matches the previous selection rules at $D = 0$, and for small D this transition always dominates. For larger D, other transition become dominant, as the value of $J_0(qD)$ decreases and higher order Bessel terms become comparable. In particular at the values where qD match a zero of the Bessel function, the corresponding transition becomes forbidden. On the right column the absorption rate is computed for a uniform distribution of atoms centered with the vortex mode, as a function of the distribution radius R. By averaging over a region, the absorption rates is smoothed, which means that for higher R transitions with higher baseline rate dominate. This computation is of particular interest as a model for effects like the uncertainty on the placement of the atom, the existence of more than one atom per vortex mode or when considering a collection of similar experimental setups.

this transition rate is dominant over a distance of the order of the wavelength of the vortex mode. This is surprising because, intuitively, one would expect that a displacement by the size of the electronic orbital, much smaller than the wavelength of radiation, would destroy any selectivity arising from the vortex mode as the orbital is no longer sensitive to the complete phase winding of the mode. Equally interestingly, is how increasing D yields a much richer set of transition rates, which is qualitatively different for different m_{vortex}. The implication of this fact is that, given a single m_{vortex} supporting system, it is possible to tune the dominant transition using the radial position of the atomic system, which provides an extra degree of freedom to control light-matter interactions. The dependence of the absorption rate with the radial displacement, for different m_{vortex}, arises from the competition of two different factors: the Bessel function term from the superposition coefficient; and the baseline absorption rate, which corresponds to the absorption rate of a particular transition, characterized by Δm, when the atom is centered in a vortex mode with OAM of $\hbar\Delta m$. The first term is responsible for the oscillatory behavior of the absorption rate, while the second determines the overall scale. Since the coefficients $J_{n-m_{vortex}}(qD)$ have zeros for various values of D, between two transitions of different Δm there are regions where one dominates over the other.

The previous discussion provides a framework for a single atomic system, whose position is known perfectly. However, in a real experimental setting there is always some inherent uncertainty associated with the position of the atom. Moreover, there are great challenges in single atom experiments arising both from the manipulation and preparation of the system, as well as the measurement of a meaningful spectroscopic signal. In real experimental settings we expect more than one atom interacting with a vortex mode, providing a more robust experimental setting as well as a greater signal.

Both experimental circumstances can be modeled through a probability distribution over the position of the atom. In this work we consider the radially uniform distribution of radius R around the vortex center, which, despite its simplicity, provides the same qualitative results as more complex, vortex centered, distributions.

In the right column of Fig.(4-1), the expected absorption rate is computed for such distributions as a function of R. The impact of the probability distribution can be understood as smoothing the single atom absorption rates, leading to two major consequences: regions of dominance of transitions where $\Delta m \neq m_{vortex}$ are moved further away from the center, making transitions with $\Delta m = m_{vortex}$ more robust; and, as we increase D, the predominance of the transitions only evolves towards transitions with larger baseline transitions rates as the oscillatory behavior from the Bessel function coefficient is averaged out.

As mentioned before, the results presented here are not characteristic of the presented transitions, but are general considerations for all sets of transitions. In order to demonstrate the robustness of the selection rules even for large Δm , which would be expected to be highly suppressed, in Fig.(4-2) we investigate the absorption of a vortex mode with $m_{vortex} = 5$. As in Fig.(4-1), the left column corresponds to the calculation of the absorption rate for a single atomic system, while the right column corresponds to the absorption rate over a uniform probability rate of radius R. On the top two plots, the case of $m_{vortex} = 1$ is considered, which provides a direct comparison to the new set of transition. The bottom two plots correspond to the $m_{vortex} = 5$ case, on which the dominance of the $\Delta m = 5$ transition is present for small radii, despite having a baseline rate much smaller than the remaining transitions. As the atom moves away from the center of the vortex, the predominant transition has smaller Δm, which corresponds to a transition with higher baseline rate, since the lower m_{vortex}, the larger the field strength near the center of the vortex mode. The same smoothing observed in Fig.(4-1) is present in this case, which allow us to predict the measured absorption rate for a given experimental atom placement uncertainty. These two plots only contain the transitions which are dominant at some radius; for a complete plot with all the transitions from $(5,0,0) \rightarrow (6,l,m)$ for $m_{vortex} = 5$, please refer to Appendix E.

In real systems, the degeneracy between levels is lifted and they are characterized by peaks of finite width, due to decaying processes. This finite width peak, may lead to the overlap of different energy states, meaning that the choice of frequency is not

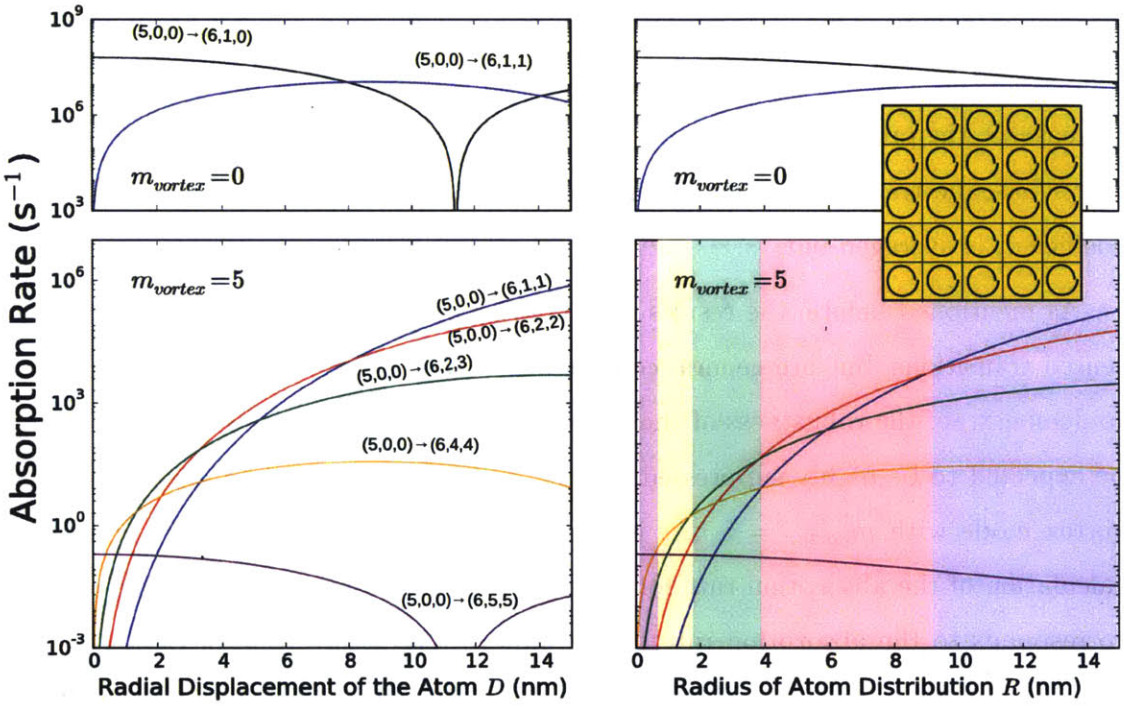

Figure 4-2: **Investigation of the single photon absorption rates for a highly suppressed transition of $\Delta m = 5$ as a function of the geometry of the system with $z_0 = 20$ nm.** Following the same organization as Fig.(4-1), on the left column, the absorption rates as function of the displacement of the atom are presented, while on the right, we are varying the radius of a uniform probability distribution over the position of the atom. Although the higher vortex transitions have much smaller transition rate, there is always a region where these transitions dominate, due to the behavior of the different order Bessel function for small argument. Although this might be a small region, it enables, for the first time, to selectively absorb into a class of electronic states through highly forbidden transition. If the region is too small it can be made larger by decreasing the confinement factor, at the expense of the absorption rate, as discussed in Section 4.3. The measured signal can be improved by performing many parallel, using slit coupling [44, 10, 11], experiments on a single substrate, as pictured in the inset schematic. A plot of the absorption rates of all possible transitions is given in Fig.(E-1)

enough to precisely transition to a particular level. OAM carrying SP(h)P modes add a new degree of freedom that enables the selection of the final state of the electronic transition, providing a higher degree of control in the experiment.

The ability to control the dominant transition through the displacement of the atom with respect to the vortex mode center adds even more flexibility to our implementation of these transitions. Consider the example of transitioning an electron from $(5,0,0) \rightarrow (6,4,3)$. The most direct approach is to develop a substrate supporting a vortex mode with $m_{vortex} = 3$ and place the atom at the center. However, for a larger m_{vortex} the masks used in the generation of these modes have a greater number of discontinuities [44, 10, 11], which correspond to an increase of edge effects resulting in a less pristine vortex mode. An alternative would be to generate a $m_{vortex} = 2$ vortex mode, and place the atom at a distance which maximizes $J_1(qD)$, which corresponds to $qD = 1.84$ and $J_1(qD) = 0.58$. Although there would be a reduction of the absorption rate to about 33% with respect to the original value vortex centered rate, this may be a smaller reduction that what would arise from the lower quality of the $m_{vortex} = 3$ mask with respect to the $m_{vortex} = 2$ mask.

4.3 Effect of Confinement Factor on Transitions on a Displaced Atom

To fully characterize the system it becomes important to also consider the impact of the confinement factor on the absorption rates and their robustness. As shown in Fig.(2) the increase in the confinement of the SP(h)P mode leads to an increase of the absorption rates of the atom due to a better coupling between the orbitals and radiation; however, it is also associated with an exponential decrease of the value of the field at the location of the atom, due to the evanescent nature of the mode. The competition between these two effects leads to a peak in the absorption rate where the exponential decrease becomes the dominating effect, as illustrated in Fig.(4-3).

Another consequence of the increase in confinement factor is the overall decrease

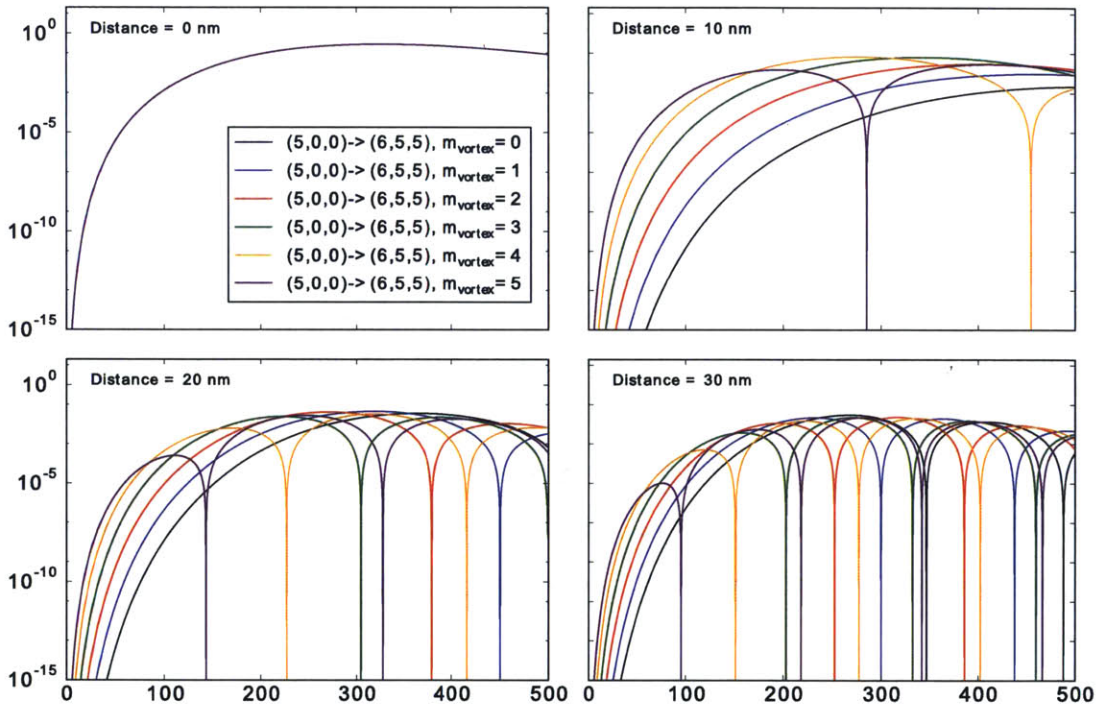

Figure 4-3: **Single Photon absorption rate as a function of the confinement factor of the system for different value of the atom's displacement away from the vortex center for $z_0 = 20\,\text{nm}$.** The higher confinement factor leads to an increase in the absorption rate until the exponential decay of the field strength becomes the dominant dominant. At the same time, the increase in confinement factor leads to a decrease of the system's length scale, as observed by the greater density of absorption rate zeros (dips) at higher confinement factors. As a result, higher confinement factor experimental setups require a higher experimental precision to ensure the atom rest in the region where the transition of interest is dominant.

in the length scale of the system, which leads to a decrease in the size of the regions where the transitions of interest dominate, requiring a greater experimental precision, as seen in Fig.(4-3) by the increase of the number of zeros of the transitions rates as we increase the confinement η. The balance between higher absorption rate and increased experimental precision is an important consideration when designing an experiment, in particular when choosing the SP(h)P supporting material.

Understanding the impact of the confinement factor in the experiment is of special interest in graphene, where the confinement factor of SPP modes can be externally tuned [6], providing an extra degree of freedom for optimizing the experimental setup.

One consideration missing from our discussion is the presence of losses in the materials, however our formalism can be generalized to include material losses as shown in a previous work [40], allowing our results to be extended to a wider range of materials.

Chapter 5

Conclusion

In this thesis we have shown how orbital angular momentum carrying polaritonic vortex modes can be used to selectively induce electronic transitions in nearby atomic systems. We showed how new selection rules, corresponding to angular momentum conservation, arise when the atom is aligned with the center of the vortex mode. In the off-centered case, we showed how the transition that conserves angular momentum ($\hbar\Delta m = \hbar m_{vortex}$) is always dominant near the center. For larger displacement radius, different transition become predominant at the length scale of the wavelength of the mode instead, as one would expect, the electronic length scale. As a result, by varying the radial position of our atomic system, a single experimental configuration is able to access a variety of novel transitions.

In the long term, the ability to engineer the electronic transitions in a quantum system, enabled by polaritonic modes, opens the doors for many applications which depend on an usually inaccessible quantum state. The study of these previously inaccessible states in simple table-top experimental setups may enable novel light emmiting devices and even lasing technologies. At the same time, including OAM carrying polariton modes in the toolbox of spectroscopists adds a new technique to target particular electronic transitions and states in atomic systems.

This work also leads directly to some interesting experimental and theoretical questions. On the experimental side, the ability of generating masks in substrates which support a single OAM carrying vortex mode has already been demonstrated

[44, 10, 11] and replicating the mask over a surface (as depicted in inset Fig.(4-3)) provides a simple experimental setup where the ideas presented in this work can be tested and further explored. On the theoretical side, it would be of interest to analyze higher-order absorption processes, in search of new methods for multi-photon absorption and emission, with a possible impact on quantum information.

Appendix A

Mathematical Description of Surface Polariton Modes

In this appendix we describe mathematically Surface Polaritons (SP(h)P), analyze the conditions for their existence and deduce their dispersion relations.

A.1 Single Interface SP(h)P Modes

Consider the geometry represented in Fig.(2-1). We are interested in describing the transverse magnetic (TM) SP(h)P mode, as the transverse electric (TE) are not present for normal parabolic materials [31]. The fields of the modes can be solved by considering an ansatz and showing that it solves Maxwell's equations in this geometry. To build this ansatz we note that each material is uniform, the field inside must be exponential (propagating or decaying) in all direction. Since we expect the mode to be propagating in the in-plane direction and evanescent in the out-of-plane direction, corresponding to the following ansatz:

$$\boldsymbol{B}_1 = B_1 \hat{q}_\perp e^{-Q_1 z} e^{i(\boldsymbol{q}\cdot\boldsymbol{\rho}-\omega t)} \text{ for } z > 0 \tag{A.1}$$

$$\boldsymbol{B}_2 = B_2 \hat{q}_\perp e^{Q_2 z} e^{i(\boldsymbol{q}\cdot\boldsymbol{\rho}-\omega t)} \text{ for } z < 0 \tag{A.2}$$

where $\boldsymbol{B}_i$ is the magnetic field in material i, $\boldsymbol{q}$ is the in-plane momentum, $\hat{q}_\perp$ is the

unit vector such that $\hat{q}_\perp \times \hat{q} = \hat{z}$, Q_i is the inverse decay length of the field in the out of plane direction for the i-th material, ω is the frequency of the mode and B_i are the overall magnitudes of the field. The in-plane momentum is the same for both the branches of the field by the translation symmetry of the system in the in-plane direction.

By the imposition that the transverse magnetic is continuous over the interface $B_1 = B_2 = B_0$, and assuming $\mu_1 = \mu_2 = \mu_0$, where μ_0 is the magnetic permeability of vacuum. The electric field can be obtained through Maxell equations:

$$\nabla \times \boldsymbol{B}_1 = \mu_0 \frac{\partial \boldsymbol{D}_1}{\partial t} \Rightarrow \boldsymbol{E}_1 = \frac{B_0}{-i\omega} \frac{1}{\epsilon_1 \mu_0} (-\hat{q} Q_1 - iq\hat{z}) e^{-Q_1 z} e^{i(\boldsymbol{q}\cdot\boldsymbol{\rho} - \omega t)} \tag{A.3}$$

$$\nabla \times \boldsymbol{B}_2 = \mu_0 \frac{\partial \boldsymbol{D}_2}{\partial t} \Rightarrow \boldsymbol{E}_2 = \frac{B_0}{-i\omega} \frac{1}{\epsilon_2 \mu_0} (\hat{q} Q_2 - iq\hat{z}) e^{Q_2 z} e^{i(\boldsymbol{q}\cdot\boldsymbol{\rho} - \omega t)} \tag{A.4}$$

By imposing that the transverse part of the electric field be continuous we can related the two sides of the interface by:

$$-\frac{Q_1}{\epsilon_1} = \frac{Q_2}{\epsilon_2} \Rightarrow -\frac{Q_1}{Q_2} = \frac{\epsilon_2}{\epsilon_1} \tag{A.5}$$

Since Q_i must be positive, so our modes are not divergent, ϵ_1 and ϵ_2 must have opposite signs for Eq.(A.5) to have a solution.

From the wave equation, in each material we obtain the relationship between Q_i and q as:

$$q^2 - Q_i^2 = \epsilon_{ri} \frac{\omega^2}{c^2} \tag{A.6}$$

where ϵ_{ri} is the relative permittivity of material i.

The dispersion relationship can be obtained by relating Eq.(A.6) for the two media, with the result being:

$$q = \frac{\omega}{c} \sqrt{\frac{\epsilon_{r1}\epsilon_{r2}}{\epsilon_{r1} + \epsilon_{r2}}} \tag{A.7}$$

where ϵ_{ri} can be frequency dependent, and c is the speed of light in vacuum. Note that to have propagating modes (q real) we also require $\epsilon_{r1} + \epsilon_{r2} < 0$.

Using a gauge where the scalar potential is zero, we can obtain the expression for

the vector potential of the upper region as:

$$\boldsymbol{A} = \frac{A_0}{\sqrt{2}}\left(\hat{q} + i\frac{q}{Q}\hat{z}\right)e^{-Qz}e^{i(\boldsymbol{q}\cdot\boldsymbol{\rho}-\omega t)} \tag{A.8}$$

In the electrostatic limit, $q \gg \frac{\omega}{c}$, $q \approx Q_i$, and the vector potential becomes:

$$\boldsymbol{A} = \frac{A_0}{\sqrt{2}}\left(\hat{q} + i\hat{z}\right)e^{-qz}e^{i(\boldsymbol{q}\cdot\boldsymbol{\rho}-\omega t)} \tag{A.9}$$

A.2 Thin film SP(h)P Modes

In the case of a thin metallic field between two dielectric materials, the procedure is the same as described in Section A.1. However, between the two materials, the existence of a metallic film enables surface current to appear, altering the magnetic field boundary conditions to:

$$\frac{\boldsymbol{B}_1}{\mu_1} - \frac{\boldsymbol{B}_2}{\mu_2} = \boldsymbol{K} = \sigma(\omega, q)\boldsymbol{E}_{\|} \tag{A.10}$$

where $\boldsymbol{K}$ is the surface current at the interface, $\sigma(\omega, q)$ is the conductivity of the film and $\boldsymbol{E}_{\|}$ is the component of the electric field parallel to the surface. For most materials the change in magnetic permeability is negligible so we consider $\mu_1 = \mu_2 = \mu_0$. Even with the presence of a surface current the parallel component of the electric field $\boldsymbol{E}_{\|}$ is continuous through the interface, which gives us the boundary condition:

$$E_{1\|} = E_{2\|} \Rightarrow B_1\frac{Q_1}{\epsilon_1} = -B_2\frac{Q_2}{\epsilon_2} \tag{A.11}$$

Combining Eq.(A.10) and Eq.(A.11), and writing $E_{\|}$ in term of either B_1 or B_2 yields the following dispersion relationship.

$$\frac{\epsilon_{r1}}{Q_1} + \frac{\epsilon_{r2}}{Q_2} = \frac{\sigma(\omega, q)}{i\epsilon_0\omega} \tag{A.12}$$

The values of Q_i can be related to the values of ω and q by the wave equation,

Eq.(A.6), yielding:

$$\frac{\epsilon_{r1}}{\sqrt{q^2 - \frac{\epsilon_{r1}\omega^2}{c^2}}} + \frac{\epsilon_{r2}}{\sqrt{q^2 - \frac{\epsilon_{r2}\omega^2}{c^2}}} = \frac{\sigma(\omega, q)}{i\epsilon_0\omega} \tag{A.13}$$

which in the electrostatic limit $q \gg \omega/c$ takes the form:

$$q = \epsilon_0 \bar{\epsilon}_r \frac{2i\omega}{\sigma} \tag{A.14}$$

where ϵ_0 is the electric permittivity of vacuum and $\bar{\epsilon}$ is the average of the electric permittivities of the two dielectric materials.

Appendix B

Derivation of the Dipole Approximation

In this Appendix we derive the dipole approximation Hamiltonian starting from the non-relativistic Hamiltonian of a particle in an electromagnetic field and analyze the allowed transitions within this approximation.

B.1 Dipole Approximation Hamiltonian

We begin by considering a gauge where the scalar potential cancels exactly, $\phi(\boldsymbol{r}) = 0$, so the Hamiltonian is given by:

$$H = \frac{1}{2m}(\boldsymbol{p} - e\boldsymbol{A})^2 + V(\boldsymbol{r}) \tag{B.1}$$

where $V(\boldsymbol{r})$ corresponds to a general potential. Although the atom's Coulomb potential has also an electromagnetic origin, we can treat it as a generic potential $V(\boldsymbol{r})$ separately from the SP(h)P mode, whose gauge we choose to have the electric potential zero, $\phi(\boldsymbol{r}) = 0$.

The simplification of the Hamiltonian arises from a gauge transformation. Let us consider some eigenfunction $|\psi\rangle$ of H. We can rewrite as a function of some other

state $|\phi\rangle$ multiplied by a factor related to the gauge of the system. If we choose:

$$|\psi\rangle = e^{ie\boldsymbol{A}\cdot\boldsymbol{r}/\hbar}|\phi\rangle \tag{B.2}$$

In this case the eigenvalue equation becomes:

$$i\hbar\partial_t e^{ie\boldsymbol{A}\cdot\boldsymbol{r}/\hbar}|\phi\rangle = \left[\frac{1}{2m}(\boldsymbol{p}-e\boldsymbol{A})^2 + V(\boldsymbol{r})\right] e^{ie\boldsymbol{A}\cdot\boldsymbol{r}/\hbar}|\phi\rangle \tag{B.3}$$

$$i\hbar\partial_t|\phi\rangle = \left[\frac{1}{2m}\left(\boldsymbol{p}+e(\nabla\cdot\boldsymbol{A})\boldsymbol{r}\right)^2 - e\boldsymbol{r}\cdot\boldsymbol{E} + V(\boldsymbol{r})\right]|\phi\rangle \tag{B.4}$$

where we used the definition of electric field generated by a vector potential:

$$\boldsymbol{E} = -\frac{\partial \boldsymbol{A}}{\partial t} \tag{B.5}$$

From Eq.(B.5) we can also determine that $\nabla\cdot\boldsymbol{A}$ is zero, since $\nabla\cdot\boldsymbol{E}$ is also zero. This leaves our Hamiltonian as:

$$H_{dipole} = \frac{1}{2m}\boldsymbol{p}^2 - e\boldsymbol{r}\cdot\boldsymbol{E} + V(\boldsymbol{r}) \quad \text{where} \quad H_{dip,int} = -e\boldsymbol{r}\cdot\boldsymbol{E} \tag{B.6}$$

For a field $\boldsymbol{E}$ which does not vary significantly within the electron's orbital length scale, the field can be approximated by a constant $\boldsymbol{E}_0$, and the interaction Hamiltonian becomes:

$$\langle s_f|H_{dip,int}|s_i\rangle = -\boldsymbol{E}_0\cdot\langle s_f|e\boldsymbol{r}|s_i\rangle \tag{B.7}$$

It is called the dipole approximation, as the interaction between the electromagnetic field and the atom can be simplified to the dipole term $e\boldsymbol{r}$ of the electron.

B.2 Dipole Approximation Selection Rules

In this section we develop the selection rules that arise from the dipole approximation.

Consider a field $\boldsymbol{E}$ oriented in an arbitrary direction. From Eq.(B.6), the transition rate between two energy levels $|n_i, l_i, m_i\rangle$ and $|n_f, l_f, m_f\rangle$ will be related to the matrix

element:

$$-e\langle n_f, l_f, m_f|\boldsymbol{E}\cdot\boldsymbol{r}|n_i, l_i, m_i\rangle \tag{B.8}$$

The matrix element will be proportional to:

$$\langle n_f, l_f, m_f|\boldsymbol{E}\cdot\boldsymbol{r}|n_i, l_i, m_i\rangle \propto \int d\phi\, d\cos(\theta)\, Y_{l_f}^{m_f*}\times$$
$$\times\,(E_x\sin(\theta)\cos(\phi)+E_y\sin(\theta)\sin(\phi)+E_z\cos(\theta))Y_{l_i}^{m_i} \tag{B.9}$$

where Y_l^m is the spherical harmonic of degree l and order m. By the completeness of the spherical harmonics, each of the trigonometric functions can be written as a sum of spherical harmonics.

$$\sin(\theta)\cos(\phi)\propto Y_1^1-Y_1^{-1}\ ,\ \sin(\theta)\sin(\phi)\propto i(Y_1^1+Y_1^{-1})\ ,\ \cos(\theta)\propto Y_1^0 \tag{B.10}$$

In particular we are interested in the angular term of the integration

$$\int d\phi\, d\cos(\theta)\, Y_{l_f}^{m_f*}Y_1^m Y_{l_i}^{m_i} \tag{B.11}$$

and understand when this term is exactly zero.

Using the orthogonality of spherical harmonics we know the term can ony be non-zero when $Y_1^m Y_{l_i}^{m_i}$ is a superposition of spherical harmonics containing $Y_{l_f}^{m_f}$. Luckily the expansion of $Y_1^m Y_{l_i}^{m_i}$ can be obtained using Clebsch-Gordan coefficients as [30]:

$$Y_1^m Y_{l_i}^{m_i}=\sum_{L,M}\sqrt{\frac{3(2l_i+1)}{4\pi(2L+1)}}\langle l_i 010|L0\rangle\langle l_i m_i 1m|LM\rangle Y_L^M \tag{B.12}$$

where $\langle l_i m_i 1m|LM\rangle$ is the overlap integral between the two single particle states with a definite $\hat{L}$ and $\hat{L}_z$ of l_i, m_i and $1, m$, with the two particle state with definite total momentum $\hat{J}=\hat{L}\otimes\hat{1}+\hat{1}\otimes\hat{L}$ of L and total z-component angular momentum $\hat{J}_z=\hat{L}_z\otimes\hat{1}+\hat{1}\otimes\hat{L}_z$ of M. By stating the problem in this framework, the results from addition of angular momentum (as discussed in introductory quantum mechanics books [17, 7]) can be used. In particular the addition of angular momentum tells

us that two particles with angular momentum l_i and 1 have a combined angular momentum that lies in $|l_i - 1| \leq L \leq l_i + 1$, which means that Eq.(B.11) is only non-zero when $l_f = l_i \pm 1$ or $l_f = l_i$. At the same time, the z projection of the angular momentum adds normally, so we know that $m_f = m_i \pm 1$ or $m_f = m_i$. Moreover looking directly at Eq.(B.11), Y_1^m is an odd function so the parity of $Y_{l_f}^{m_f *}$ and $Y_{l_i}^{m_i}$ must be different, which implies that the parity of l_i and l_f must be different. Putting all these conditions together we reach the selection rules in the dipole approximation regime:

$$\Delta l = \pm 1 \quad \text{and} \quad \Delta m = \pm 1, 0 \tag{B.13}$$

Appendix C

Vortex Mode Calculations

In this Appendix we derive the OAM carrying vortex modes as well as their properties. Using the correct normalization we also define the correct field operator for the quantum treatment of our absorption problem.

C.1 Vortex Mode Derivation

A vortex OAM carrying mode can be obtained as the superposition of planar modes coming from different angles with a phase shift linearly dependent on the incoming angle θ. Since the phase shift, when going around a circle, must match at each point modulus 2π, the vortex mode can be labeled by the winding number m of its phase shift. The resulting radiation profile becomes:

$$\boldsymbol{A}_m = \frac{1}{2\pi}\int d\theta\, A_{\boldsymbol{q}} e^{im\theta} = \frac{A_0}{2\pi\sqrt{2}} e^{-qz} e^{-i\omega t} \int d\theta\, (\cos(\theta)\hat{x} + \sin(\theta)\hat{y} + i\hat{z}) e^{iq\rho\cos(\phi-\theta)} e^{im\theta} \tag{C.1}$$

where θ is, without loss of generality, the angle formed between the in plane momentum $\boldsymbol{q}$ and $\hat{x}$, ϕ is the angle formed between the in plane position $\boldsymbol{\rho}$ and $\hat{x}$. Using the

Jacobi-Anger expansion [9], we obtain:

$$\begin{aligned}\boldsymbol{A}_m &= \frac{A_0}{4\pi\sqrt{2}} e^{-qz} e^{-i\omega t} \sum_{n=-\infty}^{\infty} \int d\theta \ \left[e^{i\theta}(\hat{x} - i\hat{y}) + e^{-i\theta}(\hat{x} + i\hat{y}) + i2\hat{z}\right] i^n J_n(q\rho) e^{in\phi} e^{i(m-n)\theta} \\ &= \frac{A_0}{2\sqrt{2}} i^{m+1} e^{-qz} e^{im\phi} e^{-i\omega t} \left[(\hat{x} - i\hat{y}) J_{m+1}(q\rho) e^{i\phi} - (\hat{x} + i\hat{y}) J_{m-1}(q\rho) e^{-i\phi} + 2\hat{z} J_m(q\rho)\right]\end{aligned} \tag{C.2}$$

Transforming into spherical coordinates yields:

$$\begin{aligned}\boldsymbol{A}_m = \frac{A_0}{2\sqrt{2}} & e^{-i\omega t} i^{m-1} e^{im\phi} e^{-qr\cos(\theta)} \times \\ & \times \Big\{ 2J_{-m}(q\rho)[\hat{r}\cos(\theta) + \hat{\theta}\sin(\theta)] + im\sqrt{2}\frac{J_{-m}(q\rho))}{q\rho}\hat{\phi} \\ & + (J_{-1-m}(q\rho) - J_{1-m}(q\rho))[\hat{\theta}\cos(\theta) - \hat{r}\sin(\theta)] \Big\}\end{aligned} \tag{C.3}$$

C.2 Orthogonality of the Vortex Modes

In this section we show that vortex modes with different values of q and m are orthogonal and find the correct normalization factor such that they are orthonormal. Using Eq.(C.2), and using the standard inner product we write:

$$\begin{aligned}\langle \boldsymbol{A}_{m,q}, \boldsymbol{A}_{n,q'} \rangle = \frac{|A_0|^2}{4} i^{n-m} & \left(\int_0^\infty dz \ e^{-(q+q')z} \right) \int_0^\infty d\rho \ \rho \int_0^{2\pi} d\phi e^{i(n-m)\phi} \times \\ & \times \{ J_{m+1}(q\rho) J_{n+1}(q'\rho) + J_{m-1}(q\rho) J_{n-1}(q'\rho) + 2J_m(q\rho) J_n(q'\rho) \}\end{aligned} \tag{C.4}$$

The angular integration equals 2π for $m = n$ and 0 otherwise, while the z integration yields $1/(q + q')$. The ρ integration diverges linearly in a fashion analogous to the normalization of momentum eigenstates in free space, meaning that our modes are normalized by the size of the system L. The correct result can be obtained by explicitly including the $1/\sqrt{L}$ per mode and using the asymptotic form of the Bessel functions of the first-kind:

$$J_\nu(x) \approx \sqrt{\frac{2}{\pi x}} \cos\left(x - \frac{\nu\pi}{2} - \frac{\pi}{4}\right) \tag{C.5}$$

And the integral becomes:

$$\langle \boldsymbol{A}_m, \boldsymbol{A}_n \rangle = \lim_{L\to\infty} \frac{|A_0|^2}{(q+q')} \frac{4\pi}{L} \int_0^L d\rho \, \frac{1}{\pi\sqrt{q'q}} \cos(q\rho)\cos(q'\rho) \tag{C.6}$$

where we removed all the phase factors from the asymptotic formula as they don't alter the average value of the product of the cosines. In the case when $q \neq q'$, the integration goes to 0 as it corresponds sum of two cosines whose average is zero. For $q = q'$, the integrand is everywhere positive and the integral is non-zero. The integral is periodic, with period $2\pi/q$, and the integral over a period is π/q, meaning that the total integral is:

$$\langle \boldsymbol{A}_m, \boldsymbol{A}_n \rangle = \lim_{L\to\infty} \frac{1}{L} 2 \frac{|A_0|^2}{q} \frac{\pi}{q^2} \frac{Lq}{2\pi} = \frac{|A_0|^2}{q^2} \tag{C.7}$$

Outside of the electrostatic limit, performing the same calculation we obtain a slightly different normalization:

$$\langle \boldsymbol{A}_m, \boldsymbol{A}_n \rangle = \frac{|A_0|^2}{qQ} \frac{1+(q/Q)^2}{2} \tag{C.8}$$

where Q is the out of plane inverse decay length.

The resulting normalized fields can be expressed as:

$$\begin{aligned} \hat{\boldsymbol{e}}_{q,l} = \frac{q}{\sqrt{L}} \boldsymbol{e}_{q,l} = & \frac{q}{\sqrt{L}} \frac{1}{2\sqrt{2}} e^{-i\omega t} i^{m-1} e^{im\phi} e^{-qr\cos(\theta)} \times \\ & \times \Big\{ 2J_{-m}(q\rho)[\hat{r}\cos(\theta) + \hat{\theta}\sin(\theta)] + im\sqrt{2} \frac{J_{-m}(q\rho))}{q\rho} \hat{\phi} \\ & + (J_{-1-m}(q\rho) - J_{1-m}(q\rho))[\hat{\theta}\cos(\theta) - \hat{r}\sin(\theta)] \Big\} \end{aligned} \tag{C.9}$$

C.3 Field Operator for Vortex Modes

Having the field profiles properly normalized enables us to build the quantum field operator. In this chapter we develop the field operator for thin film supported SPP modes. The formalism can be expanded to SPhP modes, however the physical picture does not change and its computation is less straightforward.

The most straightforward normalization condition is to equate the energy of the

vacuum to $\hbar\omega/2$, as prescribed in Eq.(2.7), by equating the energy of a vector potential with normalization $\mathcal{N}$ to $\hbar\omega/2$. From classical electromagnetism, within the electrostatic regime, the energy of the electromagnetic field in a dispersive medium is given by [36]:

$$E = \frac{1}{2}\int d\boldsymbol{r}\ \frac{d(\epsilon\omega)}{d\omega}|\boldsymbol{E}|^2 = \frac{\hbar\omega}{2} \quad \text{and} \quad \boldsymbol{E} = -\frac{\partial \boldsymbol{A}}{\partial t} \tag{C.10}$$

There are three regions whose contributions we need to account for the energy of the mode, the top material, the bottom material and the thin metalic film. We assume the dielectric materials have a constant electric around the frequency of the SP(h)P ($\partial_\omega \epsilon \approx 0$). The thin film term is more complex and we will obtain its energy contribution by considering a finite slab of thickness d and taking the limit as its thickness goes to 0.

Considering first the dielectric materials we have the energy of the mode in both dielectric materials is:

$$E_{diel} = \epsilon_0 \frac{1}{2}(\epsilon_{r1} + \epsilon_{r2})\omega^2 \frac{L}{q^2}\mathcal{N}^2 = \epsilon_0 \bar{\epsilon}_r \frac{L}{q^2}\mathcal{N}^2 \tag{C.11}$$

where $\bar{\epsilon}_r$ is the average of the relative electric permittivities of the two materials.

We now compute the energy contribution of the thin metallic film by first understanding the relationship of the conductivity and the electric permittivity of the system. In particular, the dielectric constant and the conductivity, within the Drude Model [18], can be written as:

$$\epsilon_{r,film} = \left(1 - \frac{\omega_p^2}{\omega^2}\right)\theta(d/2 - |z|) \quad \text{and} \quad \sigma = i\frac{\omega_p^2}{\omega}\epsilon_0 \tag{C.12}$$

where ω_p is the plasmon frequency of the material, θ is the heavy-side theta function which is 1 when the argument is greater than 0 and 0 otherwise, and z is the out of plane distance, where $z = 0$ is the center of the slab. In the limit of $d \to 0$,

$\frac{\theta(d/2-|z|)}{d} \to \delta(z)$. In metals, the plasma frequency is given by:

$$\omega_p^2 = \frac{n_v e^2}{m^* \epsilon_0} \Rightarrow \epsilon_{r,film} = \left(d - \frac{1}{\omega^2}\frac{n_s e^2}{m^* \epsilon_0}\right)\delta(z) \tag{C.13}$$

where n_v is the electron volume number density, n_s the electron surface number density and m^* the electron's effective mass. This process corresponds to matching the volume conductivity to the surface conductivity as we reduce the dimensionality of the film.

The energy contribution of the thin film is given by, by computing the integral.:

$$E_{film} = \lim_{d\to 0}\int dz\, \frac{1}{2}\epsilon_0 \left(d + \frac{\omega_p^2}{\omega^2}d\right)\delta(z)\omega^2 \frac{L}{q}\mathcal{N}^2 = -\frac{1}{2}i\sigma\omega\frac{L}{q}\mathcal{N}^2 = \epsilon_0\bar{\epsilon}_r\omega^2\frac{L}{q^2}\mathcal{N}^2 \tag{C.14}$$

The total energy of the electromagnetic mode is given by, using Eq.(A.14):

$$E_{total} = \frac{\hbar\omega}{2} = 2\epsilon_0\bar{\epsilon}_r\omega^2\frac{L}{q^2}\mathcal{N}^2 \Rightarrow \mathcal{N}^2 = \frac{\hbar q^2}{4L\omega\bar{\epsilon}} \tag{C.15}$$

The field operator then becomes:

$$\hat{A} = \sum_{q,l}\sqrt{\frac{\hbar q^2}{4\bar{\epsilon}\omega L}}\left(\boldsymbol{e}_{q,l}a_{q,l} + \boldsymbol{e}^*_{q,l}a^\dagger_{q,l}\right) \tag{C.16}$$

C.4 Displaced Vortex Mode Decomposition

In order to compute the radiation profile of a vortex mode displaced by $\boldsymbol{D}$, we proceed with the calculation in Section C.1 with the position at which we evaluate the plane wave fields shifted by $-\boldsymbol{D}$:

$$\boldsymbol{A}^{\boldsymbol{D}}_m = \frac{A_0}{2\pi\sqrt{2}}e^{-qz}e^{-i\omega t}\int d\theta\, (\hat{q} + i\hat{z})e^{i\boldsymbol{q}\cdot(\boldsymbol{\rho}-\boldsymbol{D})}e^{im\theta} \tag{C.17}$$

The term $e^{-i\boldsymbol{q}\cdot\boldsymbol{D}}$ can be expanded using the Jacobi-Anger formula, and the result

is:

$$\boldsymbol{A}_m^{\boldsymbol{D}} = \sum_{n=-\infty}^{\infty} i^n J_n(-qD) \frac{A_0}{2\pi\sqrt{2}} e^{-qz} e^{-i\omega t} \int d\theta \, (\hat{q} + i\hat{z}) e^{i\boldsymbol{q}\cdot\boldsymbol{\rho}} e^{im\theta} e^{in(\theta-\alpha)} =$$

$$\sum_{n=-\infty}^{\infty} (-i)^n J_n(qD) e^{-in\alpha} \boldsymbol{A}_{m+n} = \sum_{n=-\infty}^{\infty} (-i)^{n-m} J_{n-m}(qD) e^{-i(n-m)\alpha} \boldsymbol{A}_n \qquad \text{(C.18)}$$

where α is the angle $\boldsymbol{D}$ makes with the reference direction, without loss of generality set to $\hat{x}$. A displaced vortex mode is a superposition of centered vortex modes, whose superposition coefficients are given by $i^{n-m} J_{n-m}(qD) e^{-i(n-m)\alpha}$.

Appendix D

Computation of the Absorption Rate of SP(h)P modes

In this appendix the absorption rate formula is simplified so as to ease its numericall computation. Including information from the OAM carrying vortex modes described in Chap.(3) and Chap.(4), the selection rules for the atom centered absorption rates are derived. The atom displaced case is also investigated analytically and it is found that the transition rates of the displaced atom case can be easily related to the transitions of the atom centered transitions. The implementation is also discussed, with emphasis on the ideas behind the simplifications and implementation used.

D.1 Simplification of Fermi's Golden Rule

As discussed in Section 2.3.2, the absorption rates of SP(h)P vortex modes can be obtained by Fermi's Golden Rule Eq.(2.10), transcribed here for reference:

$$\Gamma_{i\to j} = \frac{2\pi}{\hbar}|\langle s_f, (n-1)_\omega|H_{int}|s_i, n_\omega\rangle|^2\rho(\hbar\omega) \tag{D.1}$$

where $|s_i\rangle$ and $|s_f\rangle$ are the unperturbed electronic states described in Eq.(2.11), and $|n_\omega\rangle$ is the field state with n excitations at energy $\hbar\omega$, described by the field operator in Eq.(C.16), and $\rho(\hbar\omega)$ is the density of states of the final field states.

In this section we are interested in simplifying this expression by accounting the particular details of our system.

D.1.1 Simplification of Matrix Element

Let us consider the interacting component of the Hamiltonian, in the gauge where the scalar potential is zero, $\phi(\boldsymbol{r}) = 0$, maintaining only one SP(h)P interaction terms:

$$H_{int} = \frac{e}{2m}(\boldsymbol{A}\cdot\boldsymbol{p} + \boldsymbol{p}\cdot\boldsymbol{A}) = \frac{e}{m}\boldsymbol{A}\cdot\boldsymbol{p} \tag{D.2}$$

This result can be simplified by expanding $\boldsymbol{p}\cdot\boldsymbol{A}$. Using Einstein's summation convention:

$$p_i A_i = -i\hbar\partial_i A_i = -i\hbar[(\partial_i A_i) + A_i\partial_i] = A_i p_i - i\hbar\nabla\cdot\boldsymbol{A} \tag{D.3}$$

Where the last term cancels since, in classical electrodynamics, the dielectric, away from the interface, is neutral.

$$\nabla\cdot\boldsymbol{A} = -\int dt\ \nabla\cdot\boldsymbol{E} = 0 \quad \Rightarrow \quad H_{int} = \frac{e}{m}\boldsymbol{A}\cdot\boldsymbol{p} \tag{D.4}$$

It is also possible to use the definition of the field profiles Eq.(C.9) to show the divergence is 0, however this argument is more physically motivated.

The matrix element is then simplified to:

$$\frac{e}{m}\langle s_f, (n-1)_\omega|\boldsymbol{A}\cdot\boldsymbol{p}|s_i, n_\omega\rangle \tag{D.5}$$

D.1.2 Density of States of Field States

Computing the density of states of a given vortex mode OAM $m\hbar$ directly from its definition we have:

$$\rho(\hbar\omega) = \frac{L}{2\pi}\int dq'\delta(\hbar\omega' - \hbar\omega) = \frac{L}{2\pi\hbar}\int d\omega'\frac{1}{|\boldsymbol{v}_g|}\delta(\omega'-\omega) = \frac{L}{2\pi\hbar}\left.\frac{1}{|\boldsymbol{v}_g(\omega')|}\right|_{\omega'=\omega} \tag{D.6}$$

where $\boldsymbol{v}_g(\omega)$ is the group velocity of the SP(h)P modes with a particular value of OAM.

In the case of SPP modes, the dispersion relationship is quadratic in ω, from Eq.(2.3) and Eq.(2.4), yielding:

$$\frac{1}{|\boldsymbol{v}_g(\omega)|} = \frac{dq}{d\omega} = \frac{2q}{\omega} \Rightarrow \rho(\hbar\omega) = \eta\frac{L}{\pi\hbar c} \tag{D.7}$$

There are two important points in this calculation:

- q can only take positive values based on the way we constructed the vortex modes, meaning that there is no $-q$ contribution at the same energy to include.
- there is no sum over the entire m label of the states since we are interested in the density of states of a particular m.

More complex $\eta(\omega)$, as in SPhP modes, give rise to a quantitatively different $\rho(\hbar\omega)$, however we will use the simpler $\eta(\omega) \propto \omega$ as it qualitatively describes SP(h)P modes.

D.1.3 Full simplification

Combining Section D.1.1 and Section D.1.2 enables us to write:

$$\Gamma = \frac{\eta\hbar}{c}\left(\frac{e}{m}\right)^2 \frac{q^2}{2\bar{\epsilon}_r\epsilon_0\omega}|\langle s_f|\boldsymbol{e}_{q,m}\cdot\nabla_x|s_i\rangle\langle(n-1)_\omega|a_{q,m}|n_\omega\rangle|^2 = \frac{\pi}{\bar{\epsilon}_r}\eta^3\omega\alpha^3a_0^2n|\langle s_f|\hat{\boldsymbol{e}}_{q,m}\cdot\nabla_x|s_i\rangle \tag{D.8}$$

where n is the number of excitations in the field, α is the fine structure constant and a_0 is Bohr's radius.

D.1.4 Atom-Centered Transitions and Selection Rules

In the case when the atom is centered with the vortex mode, the system has rotational symmetry, which implies, on the basis of symmetry as well as our calculations, that the atom eigenstates and vortex modes azimuthal dependency is of the form $e^{ip\phi}$ for

$p \in \mathbb{N}$, as corroborated by our expressions for the vortex modes, Eq.(C.9), and the electronic wavefunction, Eq.(2.11).

Since the eigenstate $|n,l,m\rangle \propto e^{im\phi}$ and $\boldsymbol{A}_m \propto e^{im\phi}$ we get:

$$\langle n_f, l_f, m_f | \hat{\boldsymbol{e}}_{q,m} \cdot \nabla_x | n_i, l_i, m_i \rangle = \int d\boldsymbol{r}\ \hat{\boldsymbol{e}}_{q,m} \cdot \left(\psi^*_{n_f,l_f,m_f} \nabla \cdot \psi_{n_i,l_i,m_i} \right) \propto$$

$$\propto \int d\boldsymbol{r}\ e^{im\phi} e^{i(m_i - m_f)\phi} \Rightarrow \begin{cases} = 0 & m \neq m_f - m_i \\ \neq 0 & m = m_f - m_i \end{cases} \tag{D.9}$$

This relationship imposes a strict selection rule on the possible electronic transitions due to the absorption of a SP(h)P mode. Note how Eq.(D.9) corresponds to a conservation law of the angular momentum projected in the axis of symmetry.

D.1.5 Atom-Displaced Transitions

The case of an atom displaced from the center of the vortex mode by $\boldsymbol{D}$, the direct connection with the vortex-centered case in Section D.1.4, through the expansion discussed in Eq.(4.1). The following argument is made within the classical electrodynamics, however it is straight forwards to generalize it to a quantum field, at the expense of a more involved derivation and without a greater physical insight. For this reason we present the classical argument.

Instead of considering the atom displaced from the vortex by $\boldsymbol{D}$, we can consider the vortex displaced from the atom by $-\boldsymbol{D}$. Using Eq.(4.1), the matrix element becomes:

$$\begin{aligned} &\frac{e}{m} \langle s_f, (n-1)_\omega | \boldsymbol{A}^{-\boldsymbol{D}}_m \cdot \hat{p} | s_i, n_\omega \rangle = \\ &= \frac{e}{m} \sum_{n=-\infty}^{\infty} i^{n-m} e^{-i(n-m)\phi_0} J_{n-m}(qD) \langle s_f, (n-1)_\omega | \boldsymbol{A}_n \cdot \boldsymbol{p} | s_i, n_\omega \rangle \\ &= \frac{e}{m} i^{\Delta m - m} e^{-i(\Delta m - m)\phi_0} J_{\Delta m - m}(qD) \langle s_f, (n-1)_\omega | \boldsymbol{A}_{\Delta m} \cdot \boldsymbol{p} | s_i, n_\omega \rangle \end{aligned} \tag{D.10}$$

where $\Delta m = m_f - m_i$ is the change in projected angular momentum. In the last step, the selection rules developed in Section D.1.4 were used to eliminate all zero

elements in the sum. This result implies that the absorption rate $\Gamma_m^{\boldsymbol{D}}$ when the atom is displaced by $\boldsymbol{D}$ from a vortex with OAM $\hbar m$ can be related to the absorption rate $\Gamma_{\Delta m}$ when the atom is centered around a vortex whose OAM matches $\hbar\Delta m$ by:

$$\Gamma_m^{\boldsymbol{D}} = |J_{\Delta m - m}(qD)|^2 \Gamma_{\Delta m} \tag{D.11}$$

D.2 Numerical Calculation Code

The numerical code used in this work has been made available in `https://github.com/Lactor/VortexModeAbsorptionRates`.

In this section the code used is described and its implementation details discussed with the goal of making the code usable by others interested in this area of Physics.

The purpose of the code is to compute the absorption rate of SP(h)P modes through Fermi's Golden rule, as in Eq.(D.8), through numerical integration. It is able to compute transition rates for plane SP(h)P modes or OAM carrying vortex modes of a given confinement factor (variable s), although it can be expanded to other modes, through the description of the appropriate vector potential profile.

D.2.1 Input and Output

The main function of the this numerical code is *AbsorptionRate_Final*, which takes as input:

- ni, li, mi - the quantum number of the initial orbital of the electron

- nf, lf, mf - the quantum number of the final orbital of the electron

- $displacement = [dxdydz]$ - the displacement of the atom with respect to the modes center. dz corresponds to the height of the atom with respect to the SP(h)P supporting material's surface.

- s - the confinement factor of the SP(h)P mode
- R - the dimensionaless integration radius for spherical and polar integrations. The value of 300 was used throughout this work, however if interested in higher order transitions this values shoul be increased so as it is larger than the exponential decay of the atomic wavefunction.
- $lvortex$ - the anguar momentum value of the vortex mode to be used. Only works for non-negative lvortex, as $lvortex = -1$ is reserved for the plane SP(h)P mode.

As an output the function returns a single value through the variable *Gamma*, which returns the value of the single photon absorption rate of an SP(h)P mode, between the states $(ni, li, mi) \rightarrow (nf, lf, mf)$.

D.2.2 Normalization

In order to work with values closer to unity, all dimensions are normalized to the Bohr radius (variable $a0$), which is the length scale of the electronic system. For clarity in the code x refers to a normalized distance while r refers to a physical distance. Working in dimensionless quantities, it is possible to define a dimensionless wavefunction and gradient (as a derivative with respect to the dimensionless quantity r/a_0), which enables our code to be more robust (less numerical problems), while at the same time making clear which terms are large or small by their comparison to 1. The dimensionless gradient is related to the dimensionful gradient by a_0^{-1}, which cancels the a_0^2 in Eq.(D.8). The only dimensionful quantity becomes the frequency of the mode.

D.2.3 Vortex Mode Implementation

The plane SP(h)P mode implementation is given directly within the body of the main function *AbsorptionRate_Final*, based on our result in Eq.(A.8) with appropriate normalization constant, while the vortex modes are defined as separate functions in the

bottom of the file *AbsorptionRate_Final.m* based on Eq.(C.3). The implementation of a displaced vortex mode is also included in the same file.

The implementation of the vortex modes transforms the dimensionless distances into dimensionful distance as the momentum values are not made dimensionless throughout the code.

There are two implementations of the vortex modes, one for the vortex mode centered with the coordinate system, and the other is for the displaced vortex mode. The former corresponds to the functions *VortexlSpX*, *VortexlSpT* and *VortexlSpP* corresponding to the $\hat{r}$, $\hat{\theta}$ and $\hat{\phi}$ components of the vector potential respectively. The latter corresponds to the *VortexLDispX*, *VortexLDispT* and *VortexLDispP*, corresponding to the $\hat{r}$, $\hat{\theta}$ and $\hat{\phi}$ components of the vector potential respectively, with respect to the center of the vortex mode. As a result to relate it to the atom's degrees of freedom, a change of basis is used to compute the inner product between the two coordinate systems.

D.2.4 Vortex Mode Calculation

Although the different modes imply the computation of a three dimensional integral, each type of mode (plane, centered vortex and displaced vortex) is computed differently.

The computation of the plane SP(h)P interaction is the most straightforward corresponding to a simple three dimensional integral in spherical coordinates. This is possible because the plasmon mode is already written in spherical coordinates which matches the spherical coordinates of the atom, so the inner product between the field and the gradient is simple since the basis vectors are orthonormal.

The computation of the centered vortex mode can be reduced to a two dimensional integral due to the rotational symmetry of the problem. The vortex mode has an azimuthal dependence which goes as $e^{im\phi}$, where $\hbar m$ is the OAM of the mode, while the wavefunction term goes as $e^{-i\Delta m\phi}$, where $\hbar\Delta m$ is the change in projected angular momentum between the initial and final state. The azimuthal integral can be done analytically and equals $2\pi\delta_{m,\Delta m}$, reducing the dimensionality of our problem and

resulting in a much faster computation.

The displaced vortex mode computation is the more involved because there is no simple analytic formula for the vector potential in the spherical coordinates of the electronic system. As a result the field is computed in the spherical coordinates whose origin matches on displaced vortex's center, and then related to the spherical coordinated centered with the electronic system by a change of coordinate matrix. As a result, the calculation is a three dimensional integral with a cumbersome integrand. Since we have related the absorption rate of a displaced vortex mode with that of a centered vortex mode in Eq.(D.11), this computation is only used as a confirmation between the numerical and theoretical work.

D.2.5 Final Computation

Having computed the interaction matrix element, the computation of the final absorption rate is straightforward based on the Eq.(D.8), returning the absorption rate in a system with a single photon in the mode of interest. The absorption rate in a system with n photon just given by n times the result given. The single photon transitions are the ones compared as they provide a meaningful comparison between different values of confinement factor.

Appendix E

Transition rates for all processes in the $(5,0,0) \rightarrow (6,m,l)$ family

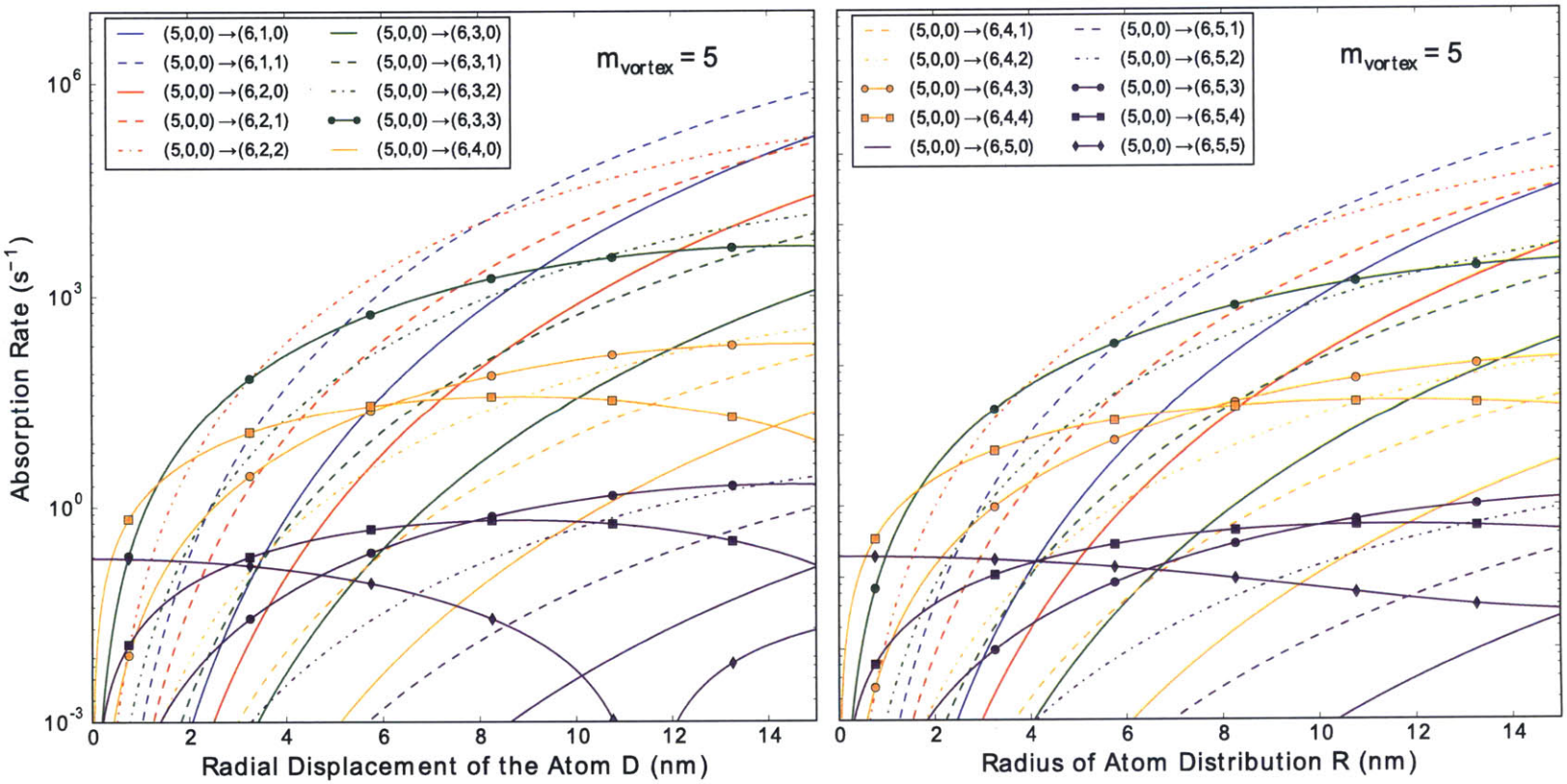

Figure E-1: **Signle photon absorption rate of a vortex mode with OAM of $5\hbar$ between the state $(5,0,0)$ and all states in the family $(6,l,m)$ with $\mathbf{z_0 = 20\,nm}$.** This plot is based on Fig.(4-2) but includes all possible transitions to states in $(6,l,m)$. By including non-dominant transitions, the competition between the baseline absorption rate and the Bessel function coefficient becomes more visible, even between transistions to the same value of l (same color). Moreover, for transitions with the same m (same linestyle), they are exactly proportional to one another (vertical translations in this log-plot), as their Bessel function coefficient is the same, and only the baseline absorption rate varies.

Bibliography

[1] L. Allen, M. W. Beijersbergen, R. J. C. Spreeuw, and J. P. Woerdman. Orbital angular momentum of light and the transformation of Laguerre-Gaussian laser modes. *Physical Review A*, 45(11):8185–8189, jun 1992.

[2] Vadym Apalkov and Mark I Stockman. Proposed graphene nanospaser. *Light: Science & Applications*, 3(7):e191, jul 2014.

[3] Konstantin Yu Bliokh, Yury P Bliokh, Sergey Savel'ev, and Franco Nori. Semiclassical dynamics of electron wave packet states with phase vortices. *Physical review letters*, 99(19):190404, nov 2007.

[4] Joshua D Caldwell, Orest J Glembocki, Yan Francescato, Nicholas Sharac, Vincenzo Giannini, Francisco J Bezares, James P Long, Jeffrey C Owrutsky, Igor Vurgaftman, Joseph G Tischler, Virginia D Wheeler, Nabil D Bassim, Loretta M Shirey, Richard Kasica, and Stefan A Maier. Low-loss, extreme subdiffraction photon confinement via silicon carbide localized surface phonon polariton resonators. *Nano letters*, 13(8):3690–7, aug 2013.

[5] Joshua D Caldwell, Andrey V Kretinin, Yiguo Chen, Vincenzo Giannini, Michael M Fogler, Yan Francescato, Chase T Ellis, Joseph G Tischler, Colin R Woods, Alexander J Giles, Minghui Hong, Kenji Watanabe, Takashi Taniguchi, Stefan A Maier, and Kostya S Novoselov. Sub-diffractional volume-confined polaritons in the natural hyperbolic material hexagonal boron nitride. *Nature communications*, 5:5221, jan 2014.

[6] Jianing Chen, Michela Badioli, Pablo Alonso-González, Sukosin Thongrattanasiri, Florian Huth, Johann Osmond, Marko Spasenović, Alba Centeno, Amaia Pesquera, Philippe Godignon, Amaia Zurutuza Elorza, Nicolas Camara, F Javier García de Abajo, Rainer Hillenbrand, and Frank H L Koppens. Optical nano-imaging of gate-tunable graphene plasmons. *Nature*, 487(7405):77–81, jul 2012.

[7] Claude Cohen-Tannoudji, Bernard Diu, and Frank Laloe. *Quantum mechanics.* 1996.

[8] Claude Cohen-Tannoudji and David Guéry-Odelin. *Advances in Atomic Physics.* 2011.

[9] David Colton and Rainer Kress. *Inverse Acoustic and Electromagnetic Scattering Theory*. 3 edition, 2013.

[10] Asaf David, Bergin Gjonaj, and Guy Bartal. Two-dimensional optical nanovortices at visible light. *Physical Review B*, 93(12):121302, mar 2016.

[11] Asaf David, Bergin Gjonaj, Yochai Blau, Shimon Dolev, and Guy Bartal. Nanoscale shaping and focusing of visible light in planar metal–oxide–silicon waveguides. *Optica*, 2(12):1045, dec 2015.

[12] Bogdan Diaconescu, Karsten Pohl, Luca Vattuone, Letizia Savio, Philip Hofmann, Vyacheslav M Silkin, Jose M Pitarke, Eugene V Chulkov, Pedro M Echenique, Daniel Farías, and Mario Rocca. Low-energy acoustic plasmons at metal surfaces. *Nature*, 448(7149):57–9, jul 2007.

[13] Luping Du and Dingyuan Tang. Manipulating propagating graphene plasmons at near field by shaped graphene nano-vacancies. *Journal of the Optical Society of America. A, Optics, image science, and vision*, 31(4):691–5, may 2014.

[14] A. Einstein. Die Plancksche Theorie der Strahlung und die Theorie der spezifischen Wärme. *Annalen der Physik*, 327(1):180–190, 1906.

[15] Z Fei, A S Rodin, G O Andreev, W Bao, A S McLeod, M Wagner, L M Zhang, Z Zhao, M Thiemens, G Dominguez, M M Fogler, A H Castro Neto, C N Lau, F Keilmann, and D N Basov. Gate-tuning of graphene plasmons revealed by infrared nano-imaging. *Nature*, 487(7405):82–5, jul 2012.

[16] Zhe Fei, Gregory O Andreev, Wenzhong Bao, Lingfeng M Zhang, Alexander S McLeod, Chen Wang, Margaret K Stewart, Zeng Zhao, Gerardo Dominguez, Mark Thiemens, Michael M Fogler, Michael J Tauber, Antonio H Castro-Neto, Chun Ning Lau, Fritz Keilmann, and Dimitri N Basov. Infrared nanoscopy of dirac plasmons at the graphene-SiO_2 interface. *Nano letters*, 11(11):4701–5, nov 2011.

[17] David J. Griffiths. *Introduction to Quantum Mechanics*. Pearson Prentice Hall, 2nd edition, 2004.

[18] Giuseppe Grosso and Giuseppe Pastori Parravicini. *Solid State Physics*. Academic Press, 2 edition, 2013.

[19] H He, ME Friese, NR Heckenberg, and H Rubinsztein-Dunlop. Direct observation of transfer of angular momentum to absorptive particles from a laser beam with a phase singularity. *Physical review letters*, 75(5):826–829, jul 1995.

[20] R Hillenbrand, T Taubner, and F Keilmann. Phonon-enhanced light matter interaction at the nanometre scale. *Nature*, 418(6894):159–62, jul 2002.

[21] Ognjen Ilic, Marinko Jablan, John D. Joannopoulos, Ivan Celanovic, Hrvoje Buljan, and Marin Soljačić. Near-field thermal radiation transfer controlled by plasmons in graphene. *Physical Review B*, 85(15):155422, apr 2012.

[22] Marinko Jablan, Hrvoje Buljan, and Marin Soljačić. Plasmonics in graphene at infrared frequencies. *Physical Review B*, 80(24):245435, dec 2009.

[23] Marinko Jablan, Marin Soljacic, and Hrvoje Buljan. Plasmons in Graphene: Fundamental Properties and Potential Applications. *Proceedings of the IEEE*, 101(7):1689–1704, jul 2013.

[24] I. Kaminer, Y. Tenenbaum Katan, H. Buljan, Y. Shen, O. Ilic, J. J. López, L. J. Wong, J. D. Joannopoulos, and M. Soljačić. Quantum \v{C}erenkov Effect from Hot Carriers in Graphene: An Efficient Plasmonic Source. oct 2015.

[25] Ido Kaminer, Maor Mutzafi, Amir Levy, Gal Harari, Hanan Herzig Sheinfux, Scott Skirlo, Jonathan Nemirovsky, John D. Joannopoulos, Mordechai Segev, and Marin Soljačić. Quantum Čerenkov Radiation: Spectral Cutoffs and the Role of Spin and Orbital Angular Momentum. *Physical Review X*, 6(1):011006, jan 2016.

[26] Young Duck Kim, Hakseong Kim, Yujin Cho, Ji Hoon Ryoo, Cheol-Hwan Park, Pilkwang Kim, Yong Seung Kim, Sunwoo Lee, Yilei Li, Seung-Nam Park, Yong Shim Yoo, Duhee Yoon, Vincent E Dorgan, Eric Pop, Tony F Heinz, James Hone, Seung-Hyun Chun, Hyeonsik Cheong, Sang Wook Lee, Myung-Ho Bae, and Yun Daniel Park. Bright visible light emission from graphene. *Nature nanotechnology*, 10(8):676–81, aug 2015.

[27] Martin P J Lavery, Fiona C Speirits, Stephen M Barnett, and Miles J Padgett. Detection of a spinning object using light's orbital angular momentum. *Science (New York, N.Y.)*, 341(6145):537–40, aug 2013.

[28] Yu Liu, R. F. Willis, K. V. Emtsev, and Th. Seyller. Plasmon dispersion and damping in electrically isolated two-dimensional charge sheets. *Physical Review B*, 78(20):201403, nov 2008.

[29] A Mair, A Vaziri, G Weihs, and A Zeilinger. Entanglement of the orbital angular momentum states of photons. *Nature*, 412(6844):313–6, jul 2001.

[30] Albert Messiah. *Quantum Mechanics*. John Wiley and Sons, Inc., 1 edition, 1961.

[31] S A Mikhailov and K Ziegler. New electromagnetic mode in graphene. *Physical review letters*, 99(1):016803, jul 2007.

[32] Mohammad Mirhosseini, Omar S Magaña-Loaiza, Malcolm N O'Sullivan, Brandon Rodenburg, Mehul Malik, Martin P J Lavery, Miles J Padgett, Daniel J Gauthier, and Robert W Boyd. High-dimensional quantum cryptography with twisted light. *New Journal of Physics*, 17(3):033033, mar 2015.

[33] Gabriel Molina-Terriza, Juan P. Torres, and Lluis Torner. Twisted photons. *Nature Physics*, 3(5):305–310, may 2007.

[34] T Nagao, T Hildebrandt, M Henzler, and S Hasegawa. Dispersion and damping of a two-dimensional plasmon in a metallic surface-state band. *Physical review letters*, 86(25):5747–50, jun 2001.

[35] A. Nicolas, L. Veissier, L. Giner, E. Giacobino, D. Maxein, and J. Laurat. A quantum memory for orbital angular momentum photonic qubits. *Nature Photonics*, 8(3):234–238, jan 2014.

[36] Frederico Dias Nunes, Thiago Campos Vasconcelos, Marcel Bezerra, and John Weiner. Electromagnetic energy density in dispersive and dissipative media. *Journal of the Optical Society of America B*, 28(6):1544, may 2011.

[37] Ekmel Ozbay. Plasmonics: merging photonics and electronics at nanoscale dimensions. *Science (New York, N.Y.)*, 311(5758):189–93, jan 2006.

[38] David Pines and David Bohm. A Collective Description of Electron Interactions: II. Collective vs Individual Particle Aspects of the Interactions. *Physical Review*, 85(2):338–353, jan 1952.

[39] R. H. Ritchie. Plasma Losses by Fast Electrons in Thin Films. *Physical Review*, 106(5):874–881, jun 1957.

[40] Nicholas Rivera, Ido Kaminer, Bo Zhen, John D. Joannopoulos, and Marin Soljacic. 2D Plasmonics for Enabling Novel Light-Matter Interactions. dec 2015.

[41] Daniel Rodrigo, Odeta Limaj, Davide Janner, Dordaneh Etezadi, F Javier García de Abajo, Valerio Pruneri, and Hatice Altug. APPLIED PHYSICS. Mid-infrared plasmonic biosensing with graphene. *Science (New York, N.Y.)*, 349(6244):165–8, jul 2015.

[42] Sheng Shen, Arvind Narayanaswamy, and Gang Chen. Surface phonon polaritons mediated energy transfer between nanoscale gaps. *Nano letters*, 9(8):2909–13, aug 2009.

[43] A. Sommerfeld. Über die Ausbreitung der Wellen in der drahtlosen Telegraphie. *Annalen der Physik*, 333(4):665–736, 1909.

[44] Grisha Spektor, Asaf David, Bergin Gjonaj, Guy Bartal, and Meir Orenstein. Metafocusing by a Metaspiral Plasmonic Lens. *Nano letters*, 15(9):5739–43, sep 2015.

[45] Andrea Tomadin, Alessandro Principi, Justin C W Song, Leonid S Levitov, and Marco Polini. Accessing Phonon Polaritons in Hyperbolic Crystals by Angle-Resolved Photoemission Spectroscopy. *Physical review letters*, 115(8):087401, aug 2015.

[46] Masaya Uchida and Akira Tonomura. Generation of electron beams carrying orbital angular momentum. *Nature*, 464(7289):737–9, apr 2010.

[47] J Verbeeck, H Tian, and P Schattschneider. Production and application of electron vortex beams. *Nature*, 467(7313):301–4, sep 2010.

[48] Jian Wang, Jeng-Yuan Yang, Irfan M. Fazal, Nisar Ahmed, Yan Yan, Hao Huang, Yongxiong Ren, Yang Yue, Samuel Dolinar, Moshe Tur, and Alan E. Willner. Terabit free-space data transmission employing orbital angular momentum multiplexing. *Nature Photonics*, 6(7):488–496, jun 2012.

[49] Achim Woessner, Mark B Lundeberg, Yuanda Gao, Alessandro Principi, Pablo Alonso-González, Matteo Carrega, Kenji Watanabe, Takashi Taniguchi, Giovanni Vignale, Marco Polini, James Hone, Rainer Hillenbrand, and Frank H L Koppens. Highly confined low-loss plasmons in graphene-boron nitride heterostructures. *Nature materials*, 14(4):421–5, apr 2015.

[50] Liang Jie Wong, Ido Kaminer, Ognjen Ilic, John D. Joannopoulos, and Marin Soljačić. Towards graphene plasmon-based free-electron infrared to X-ray sources. *Nature Photonics*, 10(1):46–52, nov 2015.

[51] Yan Yan, Guodong Xie, Martin P J Lavery, Hao Huang, Nisar Ahmed, Changjing Bao, Yongxiong Ren, Yinwen Cao, Long Li, Zhe Zhao, Andreas F Molisch, Moshe Tur, Miles J Padgett, and Alan E Willner. High-capacity millimetre-wave communications with orbital angular momentum multiplexing. *Nature communications*, 5:4876, jan 2014.

[52] Alison M. Yao and Miles J. Padgett. Orbital angular momentum: origins, behavior and applications. *Advances in Optics and Photonics*, 3(2):161, may 2011.

[53] J. Zenneck. Über die Fortpflanzung ebener elektromagnetischer Wellen längs einer ebenen Leiterfläche und ihre Beziehung zur drahtlosen Telegraphie. *Annalen der Physik*, 328(10):846–866, 1907.